

CLOSED-LOOP THRUST AND PRESSURE PROFILE THROTTLING OF A
NITROUS OXIDE/HYDROXYL-TERMINATED POLYBUTADIENE HYBRID
ROCKET MOTOR

by

Zachary W. Peterson

A thesis submitted in partial fulfillment
of the requirements for the degree

of

MASTER OF SCIENCE

in

Aerospace Engineering

Approved:

Dr. Stephen A. Whitmore
Major Professor

Dr. R. Rees Fullmer
Committee Member

Dr. David K. Geller
Committee Member

Dr. Mark R. McLellan
Vice President for Research and
Dean of the School of Graduate Studies

UTAH STATE UNIVERSITY
Logan, Utah

2012

Copyright © Zachary W. Peterson 2012

All Rights Reserved

Abstract

Closed-Loop Thrust and Pressure Profile Throttling of a Nitrous
Oxide/Hydroxyl-Terminated Polybutadiene Hybrid Rocket Motor

by

Zachary W. Peterson, Master of Science

Utah State University, 2012

Major Professor: Dr. Stephen A. Whitmore
Department: Mechanical and Aerospace Engineering

Hybrid motors that employ non-toxic, non-explosive components with a liquid oxidizer and a solid hydrocarbon fuel grain have inherently safe operating characteristics. The inherent safety of hybrid rocket motors offers the potential to greatly reduce overall operating costs. Another key advantage of hybrid rocket motors is the potential for in-flight shutdown, restart, and throttle by controlling the pressure drop between the oxidizer tank and the injector. This research designed, developed, and ground tested a closed-loop throttle controller for a hybrid rocket motor using nitrous oxide and hydroxyl-terminated polybutadiene as propellants. The research simultaneously developed closed-loop throttle algorithms and lab scale motor hardware to evaluate the fidelity of the throttle simulations and algorithms. Initial open-loop motor tests were performed to better classify system parameters and to validate motor performance values. Deep-throttle open-loop tests evaluated limits of stable thrust that can be achieved on the test hardware. Open-loop tests demonstrated the ability to throttle the motor to less than 10% of maximum thrust with little reduction in effective specific impulse and acoustical stability. Following the open-loop development,

closed-loop, hardware-in-the-loop tests were performed. The closed-loop controller successfully tracked prescribed step and ramp command profiles with a high degree of fidelity. Steady-state accuracy was greatly improved over uncontrolled thrust.

(92 pages)

Public Abstract

Closed-Loop Thrust and Pressure Profile Throttling of a Nitrous
Oxide/Hydroxyl-Terminated Polybutadiene Hybrid Rocket Motor

by

Zachary W. Peterson, Master of Science

Utah State University, 2012

Major Professor: Dr. Stephen A. Whitmore
Department: Mechanical and Aerospace Engineering

Hybrid rocket motors use a liquid oxidizer with a solid fuel to produce thrust. The thrust produced by a hybrid rocket can be controlled by changing the amount of oxidizer that is fed into the solid motor. Because hybrid rockets only have one oxidizer line, they can be easily throttled to adjust thrust levels. By nature, hybrid rocket combustion is chaotic and the thrust produced by different motors can vary significantly. The scope of this project was to produce a controller capable of keeping the thrust of a hybrid rocket motor at a set point. To demonstrate versatility in the controller, the set point was varied throughout the motor burn. Three different thrust controllers were tested; one in which thrust was measured directly using a load cell to control the thrust produced using only the liquid oxidizer, one in which the thrust of a full hybrid rocket motor was measured with a load cell, and one in which the thrust of a full hybrid rocket motor was measured indirectly with a pressure transducer. Multiple initial tests were performed without a controller in place to determine system properties that were needed to simulate and control the thrust levels. Following the uncontrolled tests, the controllers were tested. The thrust level variations were greatly reduced during the controlled tests as compared to uncontrolled tests using the same

motor configuration. Controller performance met expectations despite some limitations in the hardware used.

(92 pages)

Acknowledgments

I would like to thank Dr. Stephen Whitmore and Shannon Eilers for all of your input on this project. Without your help I could never have finished it. I would also like to recognize Jon McCulley and Andrew Bath for your help pushing the MoNSTeR cart and cleaning and preparing my motors. Last of all, I would like to thank Coordinate Pig for showing us the way and Burger Boy for teaching us to laugh and love again.

Zach Peterson

Contents

	Page
Abstract	iii
Public Abstract	v
Acknowledgments	vii
Table of Contents	viii
List of Tables	x
List of Figures	xi
Nomenclature	xiii
1 Introduction	1
1.1 On the Inherent Safety and Operational Flexibility of Hybrid Rocket Systems	1
1.2 Hybrid Motor Throttleability	4
1.3 Hybrid Rocket Throttling Literature Review	5
2 Research Objectives	11
2.1 Simulator	11
2.2 Open-Loop Testing	11
2.3 Closed-Loop Cold-Flow Testing	12
2.4 Closed-Loop Hot-Flow Thrust-Feedback Testing	12
2.5 Closed-Loop Hot-Flow Chamber Pressure-Feedback Testing	12
3 System Overview	13
3.1 Throttle Control System Component Selection and Evaluation	13
3.2 Mobile Nitrous Oxide Supply and Testing Resource (MoNSTeR) Cart	18
3.3 Data Acquisition and Automation	20
3.4 Test Motor	23
4 Closed-Loop Throttle Controller Development	25
4.1 Evaluation of Chamber Pressure and Thrust as Throttle Control Feedback Measurements	25
4.2 Control Law Development	26
4.3 Hot-Flow System Latencies and Sources	30
5 End-to-End System Simulation	37
5.1 PID Controller Gain Model	37
5.2 Servo Model	40
5.3 Oxidizer Feed Systems Response Model	40

5.4	Measurement Feedback Noise Model	43
5.5	Gain Tuning	44
6	Open-Loop Throttle Testing	49
6.1	Open-Loop Cold-Flow Testing	49
6.2	Open-Loop Hot-Flow Testing	49
6.3	Thrust and Chamber Pressure Response Time Constants	51
6.4	Thrust, Chamber Pressure, and Mass Flow Rate Calibrations	52
6.5	Thrust and Pressure Curve Fits	53
6.6	Servo Deadband Evaluation	55
6.7	Deep Throttling Hot-Flow Testing	56
7	Closed-Loop Throttle Testing	60
7.1	Cold-Flow Test Summary	61
7.2	Hot-Flow Test Summary	61
8	Conclusion	70
	References	71

List of Tables

Table	Page
4.1 Hot-flow system latencies and sources.	31
5.1 Constants used in oxidizer feed system response model.	42
5.2 ITAE ($\text{kPa}\cdot\text{s}^2$) values corresponding to plots in Fig. 5.10.	47
6.1 Curve fit coefficients for thrust, chamber pressure, and mass flow rate calibrations.	53
6.2 Exponential curve fit coefficients used in controllers.	55
7.1 Closed-loop throttle test summary.	60
7.2 Nozzle erosion during hot-flow throttle tests.	67

List of Figures

Figure	Page
3.1 Throttle control system functional block diagram.	14
3.2 (a) Percent maximum C_v vs. opening percentage for different ball valve port geometries and (b) Port area percentage vs. % MVT for a circular-port ball valve.	16
3.3 Throttle valve assembly.	18
3.4 MoNSTeR cart P&ID.	19
3.5 Instrumentation and control data flowchart.	21
3.6 Effect of isolation amplifier on load cell noise.	22
3.7 Test motor schematic.	24
4.1 Thrust time histories for previous HTPB motor variability burns.	26
4.2 General form of control loop used for closed-loop throttling.	27
4.3 Servo response time with original and modified gains.	32
4.4 Test stand frequency response to applied impulse.	35
5.1 Simulink throttling system model.	38
5.2 Simulink PID controller.	39
5.3 Simulator control loop with expanded gain section.	39
5.4 Simulator servo model.	40
5.5 Oxidizer feed system response model.	41
5.6 Thermodynamic properties used in system piping feed physics model. . . .	41
5.7 Simulator system piping model with look up tables.	44
5.8 Pressure transducer noise model.	45
5.9 PSD of simulated and real pressure transducer noise.	45

5.10	Plots of controller response to a range of gains.	46
5.11	Controller response for three different scaled valve areas.	48
6.1	Thrust during cold-flow open loop throttle test.	50
6.2	(a) Thrust and (b) chamber pressure during hot flow open loop throttle tests.	50
6.3	Normalized thrust response curves for (a) cold-flow throttling and (b) hot-flow throttling.	52
6.4	Chamber pressure, thrust and mass flow calibrations compared to experimentally measured values.	54
6.5	Experimentally derived curve fits for (a) thrust and (b) chamber pressure as a function of % MVT.	55
6.6	Results for a servo deadband test.	56
6.7	Thrust time history with video stills from deep throttle test.	57
6.8	Normalized thrust and chamber pressure during unstable combustion in deep throttle test.	57
6.9	Injector pressure ratio during deep throttle test.	59
7.1	Thrust time histories for cold-flow closed-loop tests (a) ColdFlowCL12 (b) ColdFlowCL13 and (c) ColdFlowCL14.	62
7.2	Thrust signal compared to command for Test HTPBCL1.	63
7.3	Thrust signal compared to command for for Test HTPBCL2.	64
7.4	Thrust signal compared to command for Test PressHTPBCL3.	64
7.5	Thrust signal compared to command for Test PressHTPBCL4.	64
7.6	Thrust signal compared to command for Test PressHTPBCL5.	65
7.7	Servo input voltage and position at beginning of ramp up command.	66
7.8	Control valve position during hot-flow closed-loop throttling tests.	68

Nomenclature

Roman Symbols

A	exponential curve fit scaling coefficient
a_1	experimental quadratic curve fit coefficient
a_2	experimental linear curve fit coefficient
A_n	nozzle throat area
A_v	valve port area
A_{ev}	effective throttle valve port area
A_{inj}	injector orifice area
b_1	experimental quadratic curve fit coefficient
b_2	experimental linear curve fit coefficient
c	speed of sound
c^*	characteristic velocity
c_1	experimental quadratic curve fit coefficient
C_v	valve flow coefficient
C_{dij}	injector discharge coefficient
C_{dn}	nozzle discharge coefficient
C_{dv}	valve discharge coefficient
f_c	lowpass cutoff frequency
d_f	fuel grain port diameter
d_n	nozzle throat diameter

d_p	valve port diameter
e	controller error
f_a	acoustical mode frequency
f_l	hybrid low frequency pole
F_t	thrust
F_{tf}	final thrust
F_{ti}	initial thrust
F_{tn}	normalized thrust
f_{vs}	vortex shedding frequency
h_{1-3}	enthalpies in plumbing feed physics model
I_{sp}	specific impulse
K	total compressibility factor
K_D	derivative gain
K_I	integral gain
K_P	proportional gain
l	Strouhal number characteristic length
L^*	ratio of the chamber volume to the nozzle throat area
L_c	combustion chamber length
L_f	fuel grain length
\dot{m}_i	injector mass flow rate
\dot{m}_p	mass flow rate through valve port
\dot{m}_{in}	mass flow rate through valve port in plumbing feed physics model

\dot{m}_{out}	mass flow rate through injector in plumbing feed physics model
\dot{m}_{ox}	oxidizer mass flow rate
\dot{m}_{tot}	total mass flow rate through motor
m_2	post-throttle plumbing fluid mass in plumbing feed physics model
M_B	oxidizer bulk modulus
o/f	oxidizer to fuel mass ratio
\bar{P}	average pressure in plumbing
\bar{P}_c	average chamber pressure
\bar{P}_i	average injector manifold pressure
ΔP	pressure drop across orifice
P_0	chamber pressure
P_1	oxidizer feedline pressure in plumbing feed physics model
P_2	post-throttle plumbing pressure in plumbing feed physics model
P_{0pc}	pre-combustion chamber pressure
RT	product of gas constant and fluid temperature
$R\bar{T}$	product of the average gas constant and temperature in the combustion chamber
RT_c	product of the gas constant and combustion temperature at the nozzle entrance
S	controller thrust or chamber pressure signal
s	differential operator
s_{1-3}	entropies in plumbing feed physics model
Sr	Strouhal number
t	time

T_1	oxidizer feedline temperature in plumbing feed physics model
T_2	post-throttle plumbing temperature in plumbing feed physics model
t_{tot}	total controller run time
U	Strouhal number fluid velocity
U_f	fluid velocity in fuel grain
U_v	fluid velocity through throttling valve
V_2	post-throttle plumbing volume in plumbing feed physics model
V_p	pipng volume
x	valve position
x_0	exponential curve fit offset coefficient
X_1	oxidizer feedline fluid quality in plumbing feed physics model
X_2	post-throttle plumbing fluid quality in plumbing feed physics model
X_{ox}	oxidizer quality
y	general frequency response

Abbreviations

ADN hydroxyl-ammonium di-nitrate

HAN hydroxyl-ammonium nitrate

HTPB hydroxyl-terminated polybutadiene

LOX liquid oxygen

mAh milli-Amp hours

MMH mono-methyl hydrazine

MVT maximum valve travel, see definition in Subsection 3.1.2

NHNE non-homogeneous, non-equilibrium

Greek Symbols

β_s liquid compressibility factor

η_c combustion efficiency

γ ratio of specific heats

γ_{ox} oxidizer ratio of specific heats

ω_n natural frequency

ρ density

ρ_2 post-throttle plumbing fluid density in plumbing feed physics model

ρ_g average density of gas in plumbing

ρ_l average density of liquid in plumbing

ρ_{ox} oxidizer density

τ time constant

τ_1 delay transfer function time constant

τ_2 delay transfer function time constant

τ_c combustion chamber fill time

τ_p plumbing fill time

Chapter 1

Introduction

During the past 50 years conventional launch systems have been developed to a high state of capability; however, for a variety of reasons these vehicles have become increasingly expensive to operate. Some of these reasons include manufacturing and operational complexity, safety and environmental regulations for dealing with hazardous materials, and the generally large “support army” required for flight preparations. Because of high launch performance demands on specific impulse (I_{sp}) and thrust-to-weight ratio, conventional liquid and solid-propelled rocket stages that employ highly-energetic, explosive, or toxic propellants will likely remain the systems of choice for large military-class payloads or for human spaceflight. However, there exist emerging markets, both commercial and government, that are willing to accept a lower system performance in exchange for reduced operational costs and lower environmental impact.

1.1 On the Inherent Safety and Operational Flexibility of Hybrid Rocket Systems

A key to commercial spaceflight success is the cost efficient and safe operation of large rocket motors in civilian environments. Because of the extreme risk and potentially negative environmental impact, large solid-propelled rocket motors simply cannot be operated at civilian airports. Approximately 70% of catastrophic space launch failures are attributable to the vehicle’s power plant [1]. NASA estimates that the Space Shuttle’s liquid fueled main engines will fail catastrophically once every 1530 sorties per engine and its solid rocket boosters will fail catastrophically once every 1,550 sorties per motor [2, 3]. While this level of risk is acceptable for experimental and government-operated vehicles, it is unacceptable for a potential commercial spaceflight operator.

Hybrid motors that employ non-toxic, non-explosive propellants have the potential to fulfill this market niche. The inherent safety of hybrid rocket motors greatly reduces the operational risk to a launch vehicle or any hybrid rocket propelled missile or spacecraft. According to the U.S. Department of Transportation, hybrid motors can be stored and operated without possibility of explosion or detonation [4]. Due to safer and easier ground handling; transportation, setup, and operating costs can be greatly reduced for hybrid rockets.

Current liquid bi-propellant upper stages feature cryogenic propellant that cannot be stored for any extended period of time. The vast majority of in-space propulsion is performed using hydrazine or hydrogen-peroxide monopropellants (H_2O_2) or hydrazine-derived hypergolic bi-propellants like mono-methyl hydrazine (MMH) and nitrogen tetroxide (N_2O_4).

Unfortunately, all of these propellants are powerful reducing agents that pose serious environmental concerns. Hydrazine is extremely destructive to living tissues, and is a probable human carcinogen. Exposure produces a variety of adverse systemic effects including damage to liver, kidneys, nervous system, and red blood cells [5]. In addition to these biological and toxicological impacts, toxic propellants present significant environmental dangers for the spacecraft and launch vehicle. As chemicals prone to rapidly decompose or explode when struck, vibrated, or otherwise agitated, both hydrazine and peroxide are among the most shock-sensitive chemicals listed by the U.S. Department of Transportation [4, 6].

Although procedures are in place to allow toxic propellants to be managed safely on tightly controlled military and NASA-owned flight experiments, the toxicity and explosion potential requires extreme handling precautions. Increasingly, with a growing regulatory burden, infrastructure requirements associated with toxic propellant transport, storage, servicing, and clean up of accidental releases are becoming cost prohibitive. As space flight operations continue to shift from government-run organizations to private companies and universities that operate away from government-owned test reservations, servicing payloads requiring hydrazine as a propellant becomes operationally infeasible. Extreme handling

precautions generally do not favor hydrazine as a propellant for secondary payloads.

A non-toxic, stable propellant alternative is clearly desired. Nitrous oxide (N_2O) is an inexpensive and readily available propellant that has long been considered as a potential “green” monopropellant for spacecraft applications. Despite a slight decrease in motor performance, N_2O has several advantages that make it very competitive as a hybrid rocket oxidizer.

First, N_2O has the clear advantage of being non-toxic to human tissue and is classified as non-explosive and non-flammable by the U.S. Occupational Safety and Health Administration (OSHA) [7]. Nitrous oxide exists as a saturated liquid below its critical temperature of 36.4 C, and studies performed by the USAF have demonstrated that it is virtually impossible to force a dissociation reaction with N_2O in its liquid form [8]. Unlike the highly reactive propellants described in the previous paragraphs, nitrous oxide can be handled without special precautions beyond those required for any pressurized fluid.

Second, unlike cryogenic liquid oxygen (LOX), N_2O is highly storable and allows rocket systems to be prepared far in advance of motor use. Long-term propellant storability is a requirement for in-space propulsion systems. Proposed hydrazine replacements based on aqueous solutions of hydroxyl-ammonium nitrate (HAN) or hydroxyl-ammonium dinitrate (ADN) salts are not long-term storable. The high water content of the HAN/ADN propellants makes them susceptible to freezing during periods of extended cold soak. These propellants must be temperature conditioned for space applications.

Finally, N_2O at room pressure exists in a saturated-liquid form and has a high vapor pressure exceeding 5000 kPa. This self-pressurizing property can be used to reduce complexity of propellant delivery systems. In contrast hydrazine and peroxide have vapor pressures less than 1 kPa at room temperature. HAN/ADN and LOX have essentially zero vapor pressure at storage temperature. It must be noted that the self-pressurizing property of nitrous oxide typically produces two-phase injector flow, and this property has a significant influence on the design of the throttling control system discussed in this paper. This effect will be described in detail later.

While hybrid systems generally deliver lower I_{sp} than conventional bipropellant liquid and lower volumetric efficiency than solid rockets of the same thrust level; because the propellant components remain inert until ignited within the motor chamber, hybrid rockets are inherently safer to transport, load, store, and operate. This inherent safety greatly reduces ground handling and transport costs, and can potentially lead to overall reduction in system operating costs. Unlike solid-propelled rockets, where fuel grain flaws and age-induced cracks present a significant safety issue, hybrid rockets exhibit a relative insusceptibility to grain flaws.

1.2 Hybrid Motor Throttleability

Other advantages of hybrid rockets that can potentially overcome the lower performance level include the ability to be restarted in flight and throttled over a wider range of thrust levels than conventional liquid bi-propellant systems. Hybrid propelled rocket stages are especially attractive for micro- or nanosatellite-scale launch vehicles where high thrust-to-weight ratios are not required. For nano-launcher systems the ballistic coefficients are significantly lower compared to conventional launch vehicles; consequently, lower-g acceleration profiles are preferred and lead to better-optimized launch trajectories.

Only a few specialized, very expensive launch vehicles have liquid-propelled upper stages with the ability for throttle and in-space restarts. Examples include the Lockheed Centaur II upper stage, and the Delta IV upper stage based on the Pratt and Whitney RL10B engine. These vehicles are almost universally reserved for launching expensive government-owned reconnaissance, communications, or command & control satellites.

A restartable and throttleable hybrid rocket motor could provide a safer alternative to liquid engines and a higher efficiency alternative to cold gas and monopropellant thrusters for a secondary-payload satellite, while still providing multiple-use capabilities for station keeping and orbit transfers. Additionally, an optimal thrust profile can be implemented such as a ramp up for a rocket assisted take off (RATO) of a UAV, where high initial thrust could damage the airframe, for minimal drag of a sounding rocket or launch vehicle during endoatmospheric flight, or a ramp down for controlled descent of a planetary lander.

While open-loop throttling can be accomplished with few additions to the oxidizer feed system, an open-loop throttling system cannot adjust for motor variability. In addition to motor variability induced by inconsistencies in manufacturing processes and operating conditions, hybrid rocket motors are inherently variable by nature. Hybrid rocket thrust is more closely coupled with oxidizer mass flux than with chamber pressure. Because mass flux is driven by surface friction along a turbulent boundary layer, hybrid motor thrust is inherently chaotic. Some motor variability exists even if identical motors are used under identical conditions. Closed-loop controlled throttling adds slightly more complexity to the throttling system than does open-loop throttling, but allows the throttling system to compensate for motor variability. Controlled throttling on a hybrid rocket allows for constant thrust or chamber pressure set points that greatly minimize motor-to-motor thrust variability.

A high degree of motor-to-motor variability may be acceptable for experimental vehicles but will not secure FAA certification for non-experimental, commercial spaceflight operations. Additionally, motor-to-motor variability produces significant thrust asymmetries for clustered hybrid motor configurations, which represents a significant hazard and currently precludes using multiple hybrid motors for launch vehicles. Combustion physics require a longer aspect ratio (length to width ratio) for hybrid motors when compared to their liquid and solid counterparts. Structural components associated with this high aspect ratio make building a single hybrid motor that can produce sufficient thrust and impulse to achieve orbital velocity difficult. For clustered motors, a closed-loop throttle controller can significantly reduce demand on launch vehicle aerodynamic controls and structures.

1.3 Hybrid Rocket Throttling Literature Review

The ability of hybrid rocket motor designs to be throttled has been demonstrated since the mid-1950's and open-loop throttling has been implemented on several projects [9]. The first published research documenting hybrid rocket throttling was by Moore and Berman [10]. Moore and Berman described their motor as an augmented hydrogen peroxide monopropellant thruster because it had very high oxidizer to fuel (o/f) ratios. During

preliminary testing they noted that performance increased as more of the polyethylene fuel was added and the thruster became more of a true hybrid rocket by the end of the study. The paper simply mentions that hybrid rockets can be throttled with a single valve on the oxidizer line, but gives no details about how throttling was implemented. Throttle test results were not documented. Because these tests were performed by a private company as a contract for the U. S. Army, that information was likely proprietary or classified as secret.

In the 1960's, various organizations in the United States and Europe developed throttleable hybrid rocket motors for use in sounding rockets, aerial target drones, tactical missiles, and space launch systems. During this period, most of the propellants used for hybrid rockets were very energetic and highly toxic. ONERA in France developed a sounding rocket known as Lithergol EXperimental (LEX) that used a hypergolic red fuming nitric acid (RFNA) and metatoluene diamine/nylon propellant combination [11]. The LEX rockets had an air driven solenoid valve with a programmable timer used to throttle from a peak thrust of 10 kN down to 2 kN to optimize performance during flight. Eight LEX rocket flights were performed between 1964 and 1967, all of which were successful and reached altitudes in excess of 100 km.

Two United States Air Force (USAF) programs developed throttleable hybrid rocket motors as propulsion systems for aerial target drones. The first of which, Sandpiper, used MON-25 (25% nitric oxide and 75% nitrogen tetroxide) as an oxidizer and a mixture of 10% powdered magnesium and 90% polymethylmethacrylate (PMMA) as the solid fuel. The motor was throttleable to an 8:1 turndown ratio with a peak thrust of 2.3 kN [12,13]. Motors for Sandpiper had two parallel oxidizer feed lines. One line contained a normally-open squib valve and the other contained a flow control valve that was pre-set before flight to maintain enough thrust to counteract drag at the designated cruise speed for the test. When the rocket reached its cruise speed, the squib valve was closed and the rocket was throttled by forcing all of the oxidizer through the line with the flow control valve. Three successful Sandpiper demonstration flights were performed in 1968.

The second USAF aerial drone program to use a throttleable hybrid rocket propulsion

system was a follow-on to Sandpiper known as the High Altitude Supersonic Target (HAST) program [14]. HAST had a slightly larger motor than Sandpiper that used inhibited red fuming nitric acid (IRFNA) as the oxidizer and an 80% polybutadiene/20% PMMA mixture for the solid fuel. HAST motors were throttled using a pintle valve attached upstream of the injector manifold that was actuated by a torque motor with a ball screw. For the boost phase of flight, the valve was programmed to open to 50% of peak thrust and ramp up to full throttle over 20 seconds. Following the boost phase, the valve position could be commanded manually by a remote operator. These motors were throttleable in a 10:1 range with a peak thrust of 5.3 kN. The HAST program concluded with a series of ground tests, but the HAST propulsion system was used again in the mid-1980's with a new airframe in an aerial target drone known as the Firebolt [15].

During the 1960's the United Technology Center (UTC) worked on several hybrid rocket development projects under various government contracts, including Sandpiper [16]. One project performed for the Air Force Rocket Propulsion Laboratory (AFRPL) developed a prepackaged hybrid propulsion system for use in tactical missiles [17]. This motor used a custom made oxidizer flow control system that included two pilot solenoid valves to control two main flow poppet valves on two separate distribution manifolds - a boost phase manifold and a pilot/sustain phase manifold. The motor thrust could be step throttled between 22.2 kN and 11.1 kN by switching between the boost and sustain manifolds. The motor could be restarted up to two times at either thrust level. A fuel combination of 5% boron, 30% tetraformaltrisazine (TFTA), 30% ammonium perchlorate (AP), and 35% hydroxyl-terminated polybutadiene (HTPB) designated as HFX 7808 was used with ClF_5 as the oxidizer. A series of sub- and full-scale ground tests were performed in the mid-1960's.

Another UTC project developed a high-performance hybrid motor for use in a launch vehicle upper stage [18]. The motor used the hypergolic combination of an oxygen difluoride (FLOX, OF_2) oxidizer and a lithium based fuel, and was throttleable in an 8:1 turndown ratio with a peak thrust of 22.2 kN. Ground testing was performed, but the system was never used because of the high level of toxicity of the propellants.

In the 1970's and early 1980's, no significant research was performed on hybrid rockets due to the operational success of solid and liquid rocket systems developed in the 1960's. In the mid-1980's an increasing market for commercial satellites coupled with catastrophic failures of the Challenger and a Titan III launch vehicle created a renewed interest in hybrid rockets as cheaper and safer propulsion systems for launch vehicles. During this time the American Rocket Company (AMROC) was formed. AMROC designed several throttleable hybrid rocket motors in various sizes and configurations, most of which used either LOX or nitrous oxide oxidizers with HTPB for fuel [19–23]. The H-1500, a 1112 kN thruster designed for use in the first two stages of the company's Aquila launch vehicle could be throttled by varying the flow rate to the gas-driven turbo pumps used to pump the motor's liquid oxygen oxidizer [24]. The H-30 motor to be used as the Aquila's fourth stage featured a nitrous oxide blow-down feed system that modulated thrust using a single throttling valve in the feedline. AMROC also developed a small-scale motor to demonstrate the versatility of hybrid rockets that used Italian salami as the fuel and was throttleable to a 5:1 turndown ratio. It was quite possibly the first commercially-produced rocket described as having a “delicious BBQ flavor.”

Following the Space Shuttle Challenger accident in 1986 [9], NASA began the Hybrid Propulsion Technology Program to investigate hybrid rocket boosters as a safer alternative to the Space Shuttle's Reusable Solid Rocket Motor (RSRM) boosters [25–29]. A large-scale motor was designed to produce 4448 kN of thrust and a 1/4-scale motor to be used in a cluster of four were both evaluated with different oxidizers and fuels. Two oxidizer delivery concepts were developed, one using a pressure-fed system and the other using a pump-fed system. Both concepts had an oxidizer line that branched into four smaller lines before entering the motor. The pressure-fed system was designed with four individually throttleable valves for the four branches of the feedline and was designed to have a 1.6:1 turndown ratio. The pump-fed system was throttled in a 2.4:1 ratio by altering the fluid flow to the gas-driven turbo pumps on the feedline branches.

In the mid-1990's, NASA began the Joint Government/Industry Research and Development (JIRAD) Program with several industry partners [30,31]. The program evaluated two hybrid rocket booster sizes that were smaller than those investigated by the Hybrid Propulsion Technology Program. The first series of tests was performed using an 11 inch diameter motor that produced 13.3 kN of thrust. A larger 24 inch diameter motor that produced 178 kN of thrust was used for the second series of tests. Both motor sizes had dual oxidizer feedlines with binary-operation valves and were step throttled by closing one of the oxidizer valves. Either gaseous oxygen (GOX) or LOX was used as the oxidizer with a fuel formulation (designated as UTF-29901) that was mostly polycyclopentadiene and HTPB. Both series of tests included both steady-state and throttled motor burns.

The Hybrid Sounding Rocket (HYSR) project that began in 1999 was a cooperative effort between Lockheed Martin and Marshall Space Flight Center with the goal of producing a single stage hybrid sounding rocket to replace the two and three stage sounding rockets that were being used at the time [32]. HYSR motors used LOX with aluminized HTPB as the fuel. Like the JIRAD motors, the HYSR motors had two branching oxidizer lines and could be step throttled by closing the ball valve on one of the lines. A series of static tests was performed and the project ended with a test flight from Wallops Flight Facility in 2003.

More recently, several academic institutions have developed throttleable hybrid rockets. The University of Arkansas at Little Rock (UALR) developed a lab scale hybrid rocket motor that was used to perform plume spectroscopy experiments. The oxidizer delivery system could throttle the mass flow rate of the oxidizer between 18 and 37 g/sec using a Teledyne-Hastings HFC307 mass flow controller [33]. Stanford University developed a custom-made throttling plate for the Peregrine sounding rocket that mates to the injector face inside the injector manifold [34,35]. The plate is rotated to control the oxidizer mass flow rate between 50-100% of the nominal value. A series of static test fires performed at Purdue University demonstrated a throttle-down profile analogous to a powered descent/landing profile and a square wave profile analogous to a boost/sustain/boost profile that would be used for a tactical missile flight [36]. Throttling with a turndown ratio of 10:1 was accomplished using

a Habonim control valve with a linear flow profile.

Chapter 2

Research Objectives

The objectives for this research are to:

- Create a simulator to tune gains and predict controller response
- Classify system parameters using open-loop throttling tests on both a cold-gas system and a N_2O -HTPB hybrid rocket motor
- Evaluate thrust stability limits while deep throttling a N_2O -HTPB hybrid rocket motor
- Demonstrate closed-loop thrust control on a cold-gas N_2O system
- Demonstrate closed-loop thrust control on a N_2O -HTPB hybrid rocket motor using load cell feedback
- Demonstrate closed-loop chamber pressure control on a N_2O -HTPB hybrid rocket motor using pressure transducer feedback

2.1 Simulator

A simulator was necessary to provide an immediate prediction of system behavior. Using a simulator to predict the controller response for various settings eliminated extraneous system classification testing. Gains could also quickly be tuned by sweeping the controller through a series of gains and simulating the response for each set of gains. The simulator was coded using MATLAB/Simulink and is discussed further in Chapter 5.

2.2 Open-Loop Testing

System parameters such as time constants of step-input responses, valve opening ranges, and instrument noise were determined through open-loop testing. An open-loop deep throttle test was performed to evaluate the limits of stable thrust in the test motors. Open-loop tests were performed by programming predetermined servo position set points using Lab-

VIEW. Further discussion of specific tests performed and data taken is found in Chapter 6.

2.3 Closed-Loop Cold-Flow Testing

The first series of closed-loop throttle tests was performed on a nitrous oxide cold-gas system. Cold-flow tests were performed first because of their reduced cost and complexity. Multiple tests could be performed in succession without replacing fuel grains and ignitors, making it easier to compare results from multiple gain sets to simulator results. A thrust command profile was programmed using LabVIEW and thrust feedback was provided using a load cell on the test apparatus thrust stand. The cold-flow controller is discussed in more detail in Section 4.2. An outline of cold-flow test results is found in Section 7.1.

2.4 Closed-Loop Hot-Flow Thrust-Feedback Testing

Following cold-flow testing, a thrust-feedback closed-loop throttle controller was demonstrated on a N_2O /HTPB hybrid rocket motor. Much of the controller setup was the same as for the cold-flow tests. Only the thrust profile used in the simulator and controller and the gains used for the controller needed to be altered. The same LabVIEW program used for cold-flow testing was used for thrust-feedback hot-flow tests. More details about the controller are located in Section 4.2 and test results are found in Subsection 7.2.1.

2.5 Closed-Loop Hot-Flow Chamber Pressure-Feedback Testing

Chamber pressure-feedback tests followed the thrust-feedback tests. The LabVIEW program was modified to receive feedback data from the chamber pressure transducer instead of the thrust stand load cell. The same basic form of controller was used as for the thrust-feedback controllers with the appropriate terms modified for chamber pressure. Further discussion about the chamber pressure-feedback controller is found in Section 4.2. Test results are outlined in Subsection 7.2.2.

Chapter 3

System Overview

Control laws used in the throttle control system were greatly influenced by the hybrid motor oxidizer feed system and motor configuration. Much of the infrastructure needed to perform throttle testing already existed at USU prior to this study [37–39]. New piping and instrumentation were added to the existing test stand to incorporate the throttle control system. All of the other necessary instrumentation and hardware remained unchanged from previous research projects. This section describes the design and development of the throttling system hardware and its influence on the control algorithms.

3.1 Throttle Control System Component Selection and Evaluation

Figure 3.1 shows a functional block diagram of the throttle control system and the signal flow between each. An automation controller is used to send a positioning signal to a valve actuator, which repositions the valve to the command position. The position of the control valve determines the sensed thrust or chamber pressure, which is sent to the automation controller to finish the signal flow loop in the throttle control system.

Parameters considered during valve selection were 1) range of control authority, 2) weight, 3) cost, 4) availability, and 5) linearity of flow profile. Because of cost and schedule limitations, much of the hardware was not flight weight; however, when convenient and affordable flight weight hardware was used. The valve needed to provide control authority through typical operational ranges and still be able to reach nominal thrust levels when fully open. Because the controller could be made to handle nonlinear flow profiles, flow profile linearity was considered but was given low priority. A highly nonlinear flow profile creates precision problems in flow regions where small changes in valve position make large changes in thrust, and delays in regions where large changes in valve position are required

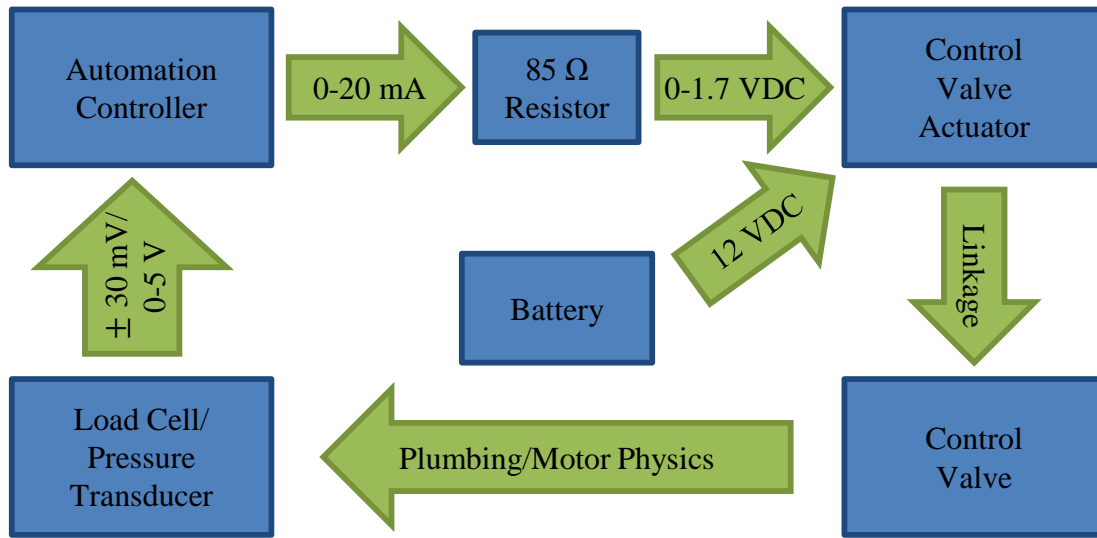


Fig. 3.1: Throttle control system functional block diagram.

to modulate thrust. Control laws are more straightforward and robust if the valve flow profile is linear, but a controller that can handle nonlinear flow profiles should be able to easily handle linear flow profiles. Matching the remote control actuator to the control valve is a key element of the design process. Parameters considered when choosing an actuator included 1) weight, 2) torque capacity, 3) power requirement, and 4) actuation speed. The actuator needed to be able to position the control valve quickly and accurately with minimal bulk and weight. A flight-weight throttling system requires the valve actuator and power supply to be lightweight and compact.

The following subsections will describe the systems engineering process used to select and size the control valve and accompanying actuator.

3.1.1 Control Valve Type Selection

Many valve types were considered during the control valve selection process. Pintle valves are the valve of choice for most aerospace throttling applications and have long been in use in air-breathing and liquid fuel rocket engines and have even seen previous use in hybrid rockets [40]. However, typically pintle valves are custom made for an application and were considered cost prohibitive for this initial evaluation project. More conventional

valve designs were considered.

Globe and gate valves have a wide range of control authority and their orifices can be shaped to provide linear throttling, but linear actuators are required for quick actuation [41]. With linear actuators globe and gate valves are quite large and would never be considered for flight applications. Other valve types that would require pulse width modulation (PWM) such as solenoid, diaphragm, and pinch valves were also considered. The nature of a PWM controller can cause rapid, repeated hard starts which increases the probability of rupturing the motor case. These valve types were held in reserve as options to be considered only if less risky control valve options prove ineffective. Ball and butterfly valves are cheap, widely available, and due to their rotary actuation make size- and weight-efficient control valves. Of these types, ball valves are more common and are available with a wider variety of port geometries for control applications, and were chosen for the control valve.

3.1.2 Control Valve Sizing

Several approaches for reducing the weight of the control valve were examined. Valves made from titanium or aluminum are much lighter than steel, but also considerably more expensive and have a more limited selection. Aluminum valves typically have lower operational pressures than were necessary for this project. A compromise that allows significant weight reduction at moderate cost was to use a steel valve with the amount of steel in the body minimized. Criteria used to minimize the amount of steel in a valve include port geometry that maximizes flow rate and the smallest valve size that could handle the required flow rates. Preference was given to low-profile versions of the valves that met the other two criteria.

Figure 3.2a shows how the percentage of the maximum flow coefficient changes with the % MVT of the valve for several different ball valve port geometries [42,43]. For brevity throughout this document, valve positions will be defined as a percentage of the maximum travel distance of the valve. For a ball valve, the maximum valve travel (MVT) is 90° and the valve position is reported as 0%-100% MVT, corresponding to a 0° - 90° rotation. The flow coefficient, C_v , is a constant that relates the geometry to the flow capacity of a valve.

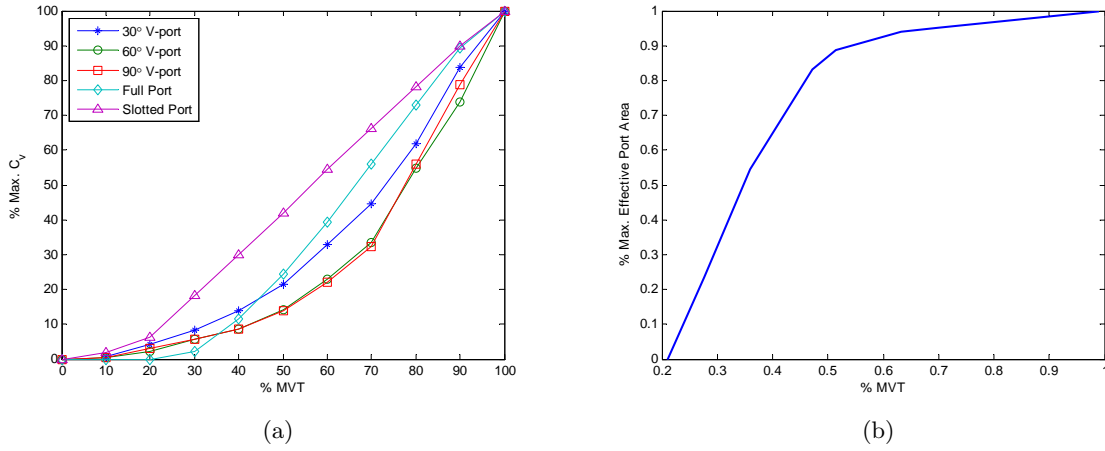


Fig. 3.2: (a) Percent maximum C_v vs. opening percentage for different ball valve port geometries and (b) Port area percentage vs. % MVT for a circular-port ball valve.

Here it is defined as the number of U.S. gallons of 60°F water per minute that will travel through a valve with a 1 psi pressure drop. For linear control over a wide range, a slotted-port ball valve is ideal but the lower maximum C_v requires a much larger valve to achieve the required flow rates compared to the wider port geometries. While C_v is the industry standard to represent the flow rate capacity of a valve, the effective port area provides a better representation of the linearity of a valve's flow profile. Figure 3.2b shows the effective port area as a function of valve position for a full-port ball valve. Although the flow profile of a circular-port ball valve is nonlinear, the open port provides the most weight efficient flow control ball valve. Because demonstration of throttling control using a flight-weight valve was desired, a standard circular-port ball valve was ultimately selected as the control valve.

The valve was sized so that the pressure drop through the port was not sufficient to cause cavitation with the valve fully open. This was mainly done to minimize flow losses and prevent unpredictable flow regimes during non-throttled tests. During warmer months, the feedline pressure stays approximately 140 kPa above the saturation pressure of nitrous oxide. To provide a safe margin, a pressure drop no more than 50 kPa was allowed through the throttling valve when fully open. The port diameter required to maintain a given

pressure drop is given by [44]

$$d_p = \sqrt{\frac{4\dot{m}_p}{\pi C_{dv}\sqrt{2\rho\Delta P}}}, \quad (3.1)$$

where \dot{m}_p is the mass flow rate through the port, C_{dv} is the discharge coefficient of the valve, ρ is the fluid density, and ΔP is the pressure drop across the valve. Assuming a discharge coefficient of 0.8 for the valve, a 7.8 mm orifice is required. The closest low-profile valve found was a 1/2" valve with a 5/16" (7.9 mm) orifice sold by McMaster-Carr.¹ The actual discharge coefficient was closer to 0.7 and the pressure drop was around 70 kPa, but was still within the acceptable limit.

3.1.3 Control Valve Actuator

The actuator chosen for the control valve was an Invenscience LC Torxis Servo i00600² rotary servomotor with a built-in Pololu jrj 21v3³ position controller. A servo was chosen as the actuator because they see typical use in RC aircraft and robotics applications that require mobility; hence they are small, light, fast, and are designed to run on battery power. Most commercial control valve actuators are designed for longevity in varying conditions. They tend to be large, relatively slow, and require more power input than could be provided by a battery.

The servo is capable of producing 1600 oz-in (11.3 N-m) of continuous torque at 12 VDC and 3200 oz-in (22.6 N-m) of peak torque with a peak current draw of 3 A. The peak torque output is approximately four times the static opening torque of the valve at the oxidizer feed pressure, which insures that valve damping will not hinder the speed of the controller. A custom mounting bracket and linkage were designed to attach the servo to the valve. The servo can be controlled by either a PWM or 0-5 VDC analog input command signal. The 0-5 VDC analog servo input corresponds to a 0°-270° full range of servo rotation.

For convenience, power is provided by a 12-volt lead acid battery for static testing.

¹McMaster-Carr Item# 45395K105, <http://www.mcmaster.com/#catalog/118/433/=i4e9p2>

²http://www.invenscience.com/index_files/Page923.htm

³<http://www.pololu.com/catalog/product/1392>

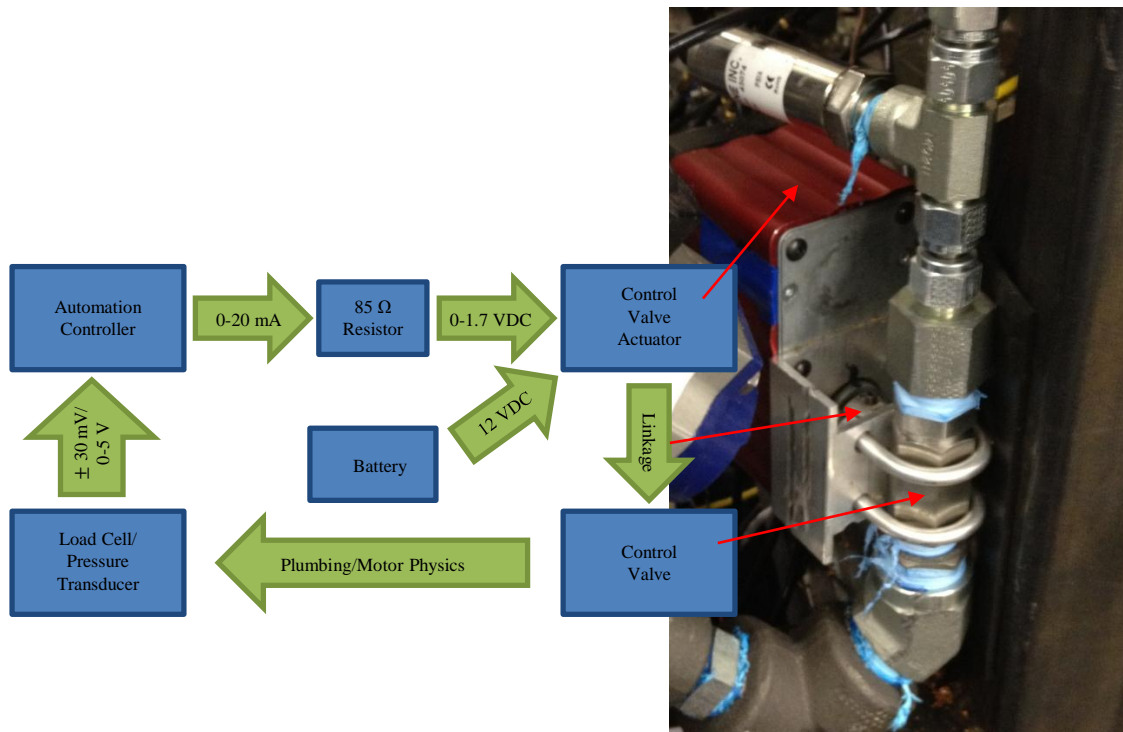


Fig. 3.3: Throttle valve assembly.

However, even at peak draw the servo only requires 36 Watts of power. Controlling thrust for one minute of powered flight at peak current draw would require a battery with rated to 50 mAh. It could be powered by a lithium polymer battery that weighs only a fraction of a kilogram. Weighing in at about 1 kg, the valve and servo assembly is potentially flight weight. Figure 3.3 shows the throttle valve assembly as it fits into the functional block diagram in Fig. 3.1. Figure 3.4 shows the relation between the throttle valve assembly and the rest of the test cart system piping.

3.2 Mobile Nitrous Oxide Supply and Testing Resource (MoNSTeR) Cart

All of the equipment required for hybrid motor testing could not be permanently stored in the test cell where static motor testing takes place because it is a shared resource and partially open to the environment. Everything required for static motor tests was built onto a cart that could be removed from the test cell and stored elsewhere. The Mobile Nitrous oxide Supply and Testing Resource (MoNSTeR) cart was custom built for hybrid

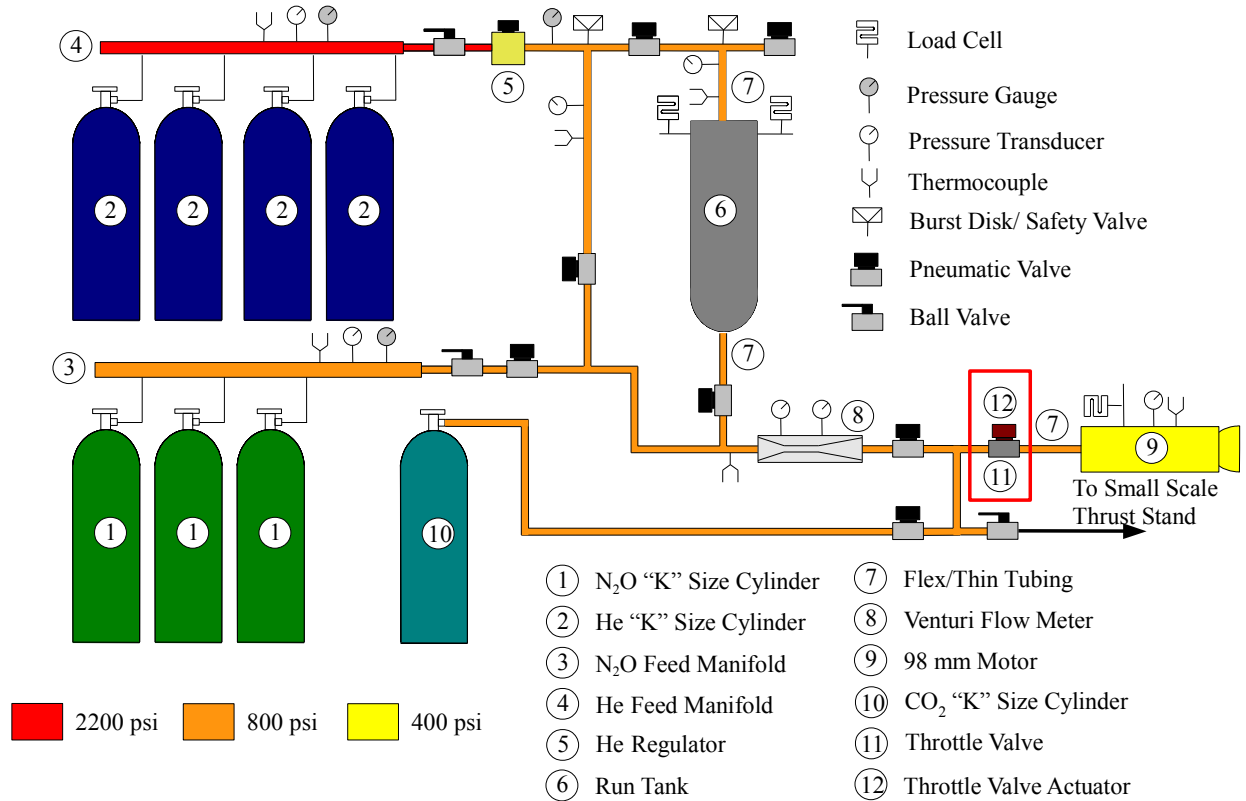


Fig. 3.4: MoNSTeR cart P&ID.

rocket research at Utah State University (USU). Figure 3.4 shows the piping and instrumentation diagram (P&ID) for the hybrid motor test arrangement with the throttling valve highlighted. The MoNSTeR cart features an oxidizer delivery system, a modular thrust balance platform, and all of the associated system piping, instrumentation, and hardware required for hybrid rocket testing.

To allow sufficient mass flow rates with minimal line losses, a predetermined mass of N₂O oxidizer, nominally 500 g/s of burn time, was delivered to a closely coupled “run tank” from a series of “K” sized industrial pressure cylinders. Nitrous oxide vapor pressure is highly dependent on temperature. Because the test cell is open to the environment, the vapor pressure of the nitrous oxide in the MoNSTeR cart’s run tank can be below saturation pressure if not controlled. Thus, the run tank was pressurized by gaseous helium (He) to insure a constant feed pressure during the entire length of the burn. The He “top pressure”

was set by a manual regulator and was maintained near 5650 kPa for throttling tests.

The top pressure keeps the N_2O above saturation pressure for the entire run and insures a single-phase liquid flow through the throttle valve for any expected ambient temperatures. The design motor chamber pressure was 2760 kPa. A pneumatic run valve upstream of the throttle valve was triggered by an electronic solenoid valve, and was automatically controlled by the instrumentation software.

Oxidizer mass flow was sensed by two vertical Omegadyne[®] LCCD-100 (445 N) load cells mounted on the run tank, and by an inline Venturi flow meter mounted in the oxidizer feed-line just ahead of the run valve. Differential Venturi flow meter pressure was measured using twin Omegadyne[®] PX409-1.0KA5V (0-6900 kPa) absolute pressure transducers. Axial load was sensed by an Omegadyne[®] LCCD-500 (2225 N) load cell and chamber pressure was sensed using an Omegadyne[®] PX409-1.0KA5V (0-6900 kPa) absolute pressure transducer mounted to the motor cap. An Omegadyne[®] Type-K thermocouple was mounted at the aft-end of the motor case to sense motor case temperature and thermal soak-back following the end of the burn. All instrumentation was excited using a 10 VDC power source. The output response for the load cells is 3 mV/Volt, and 0-5VDC for the pressure transducers.

The motors were mounted in a thrust balance on the MoNSTeR cart. A motor mounting bracket in the thrust balance is supported on the sides by five ball and clevis joint linkages, two in the vertical and three in the horizontal direction. Motion is constrained in the vertical and horizontal directions and rotations are constrained about all three principal axes by the linkages. The axial load cell is attached between the fore end of the motor mounting bracket and a rigid thrust beam using ball and clevis joints on either side. Linkages and the axial load cell were aligned to within 0.2° of the principal axes using precision squares and inclinometers.

3.3 Data Acquisition and Automation

Two National Instruments data acquisition (DAQ) systems and control devices manage

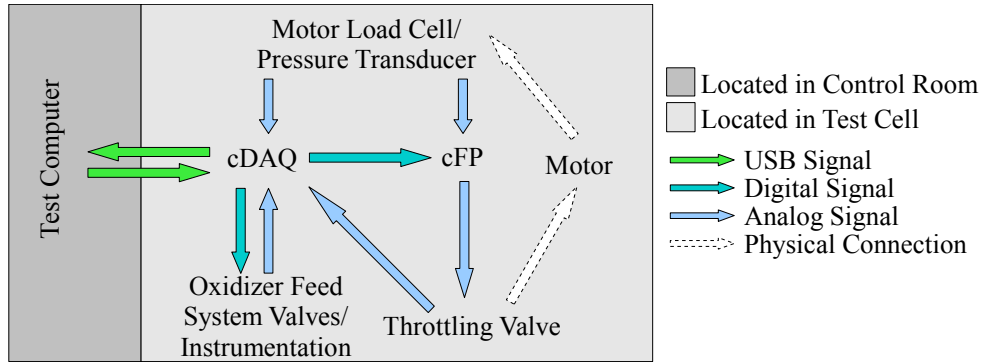


Fig. 3.5: Instrumentation and control data flowchart.

motor fire, control throttling, and log test data. An NI-compact DAQ[®] 9174⁴ (cDAQ) 4-slot bus controller with multiple analog input (16-bit), analog output, digital output, and thermocouple modules (24-bit) manage the majority of the measurements and valve control. A National Instruments Compact Fieldpoint 2020⁵ (cFP) automation controller is used to manage the throttling valve controllers. An analog input module on the cFP allows input measurements of thrust and chamber pressure for control loop feedback and to receive communication signals from the cDAQ. Operators and experimenters are remotely located in a secure control room separated from the test area. Communications to the test stand are managed by an operator-controlled computer via universal serial bus (USB) using amplified extension cables. General control and measurement functions are controlled by a LabVIEW[®] virtual instrument (VI) hosted on the control computer. A separate throttle valve controller VI was run on the cFP. Controller data was stored locally on the cFP and retrieved following the test. Figure 3.5 presents a flowchart showing the communication signals between the instrumentation and control devices.

The cFP automation controller was used to position the servo. The servo has a 270° total rotation range, but only 90° was required to actuate the control valve. The 0-20 mA signal output of the 12-bit cFP analog output module was converted to a 0-1.7 VDC input (5/3 of the 0-5 VDC command input for the 270° total range) for slightly over 90° of control authority over the valve with a 0.022° resolution. The current to voltage

⁴<http://sine.ni.com/nips/cds/view/p/lang/en/nid/207535>

⁵<http://sine.ni.com/nips/cds/view/p/lang/en/nid/11572>

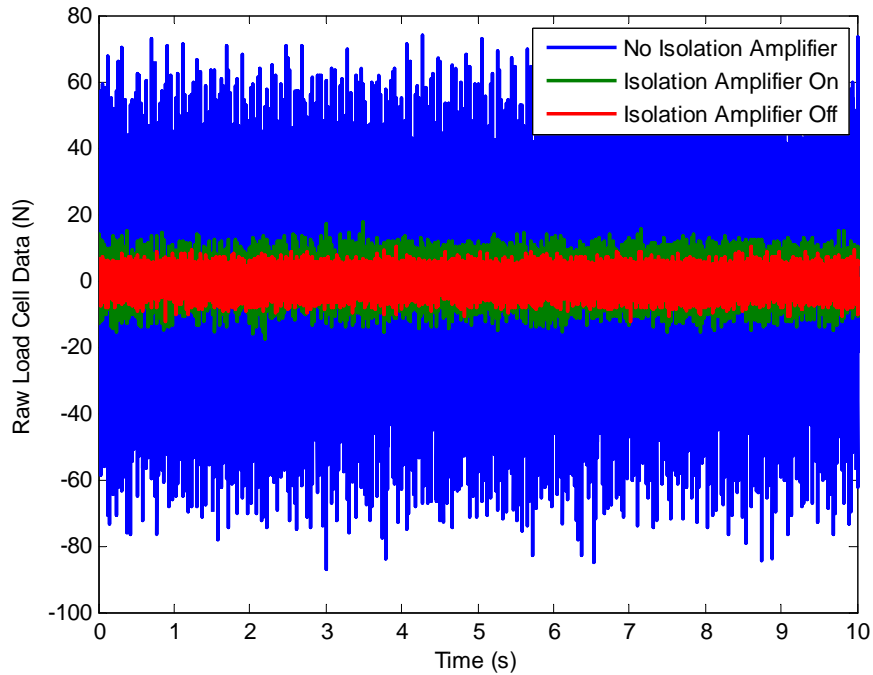


Fig. 3.6: Effect of isolation amplifier on load cell noise.

conversion of the analog output module control signal was accomplished by placing an $85\ \Omega$ resistor in series with the signal wire. Position feedback of the servo to the cDAQ was provided by an internal rotary potentiometer.

After wiring the instrumentation circuits into the cFP, it was discovered that noise from the cFP was being fed back to the cDAQ through the load cell wires. In order to preserve the noise level in the cDAQ data, an isolation amplifier circuit was placed between the cFP and the cDAQ. Figure 3.6 shows the noise level of the load cell as recorded by the cDAQ. Three cases are shown: 1) noise level without the isolation amplifier wired in (cFP wired straight to cDAQ), 2) noise level with the isolation amplifier wired in and turned on, and 3) noise level with isolation amplifier turned off (no connection between cDAQ and cFP). With the isolation amplifier turned on there is a 66% increase in signal standard deviation over that of the signal without the cFP in the circuit. Without using the isolation amplifier there is a 790% increase.

3.4 Test Motor

For these tests a commercially available Cesaroni 98-mm solid-rocket motor was modified by replacing the original motor cap with a custom-designed motor cap with a single port oxidizer injector. A threaded pressure transducer port was also installed in the motor injector cap to allow for chamber pressure measurements. The stock nozzle holder was replaced by a custom nozzle holder with a nozzle that had a larger throat diameter than the stock nozzle holder could support. To reduce run-to-run variability due to nozzle erosion, nozzles fabricated from a single piece of high-density graphite replaced the original manufacturer-supplied phenolic nozzle.

The nozzle has a 4.2:1 expansion ratio and has a design throat diameter of 1.7 cm. Two Estes “mini A” class 10-gram solid rocket motors were inserted into the injector cap as ignitors. Electronic matches burned by a 12 volt DC signal ignited these small motors. The ignitors were replaced after each test firing. Additional advantages provided by this configuration are a ready-made flight-weight motor and the ability to rapidly reload between motor tests.

HTPB fuel grains were cast using the commercially available Sartomer Poly bd[®] R-45M polybutadiene resin and PAPI 94[®] MDI curative. Sartomer R-45M has a polymerization factor of approximately 50 and a molecular weight of 2800 kg/kg-mol [45]. PAPI 94 is a polymethylene polyphenylisocyanate produced by Dow[®] Plastics Inc [46]. The formulation contains methylene diphenylene diisocyanate (MDI) in proprietary proportions. The curative has an average molecular weight of 290 kg/kg-mol. The nitrogen, carbon, oxygen (N-C-O) bonds in the MDI react with the hydroxyl (OH) terminations in the polybutadiene resin to cure the fuel grain.

For these tests carbon black was added to the mixture to insure opaqueness and prevent radiative heating of the fuel grain and motor case liners. HTPB/MDI/carbon black mass proportions were set at 87%/ 12.5%/ 0.5%, respectively. Past experience has determined that these proportions assure adequate fuel grain cure and material hardness. The resin and curative were mixed in a commercial paint mixer that was sealed and fitted so that the fuel

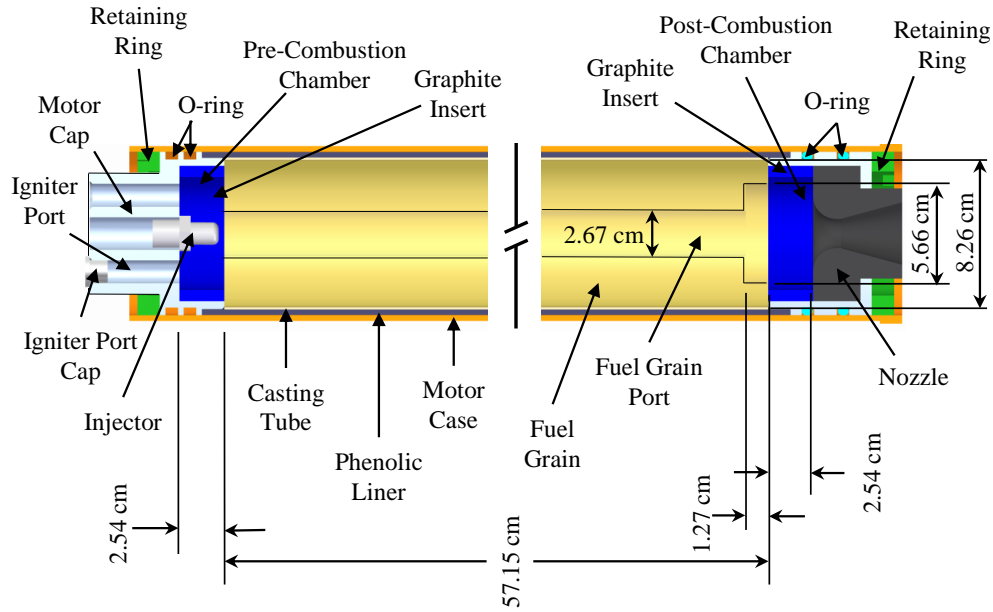


Fig. 3.7: Test motor schematic.

mixture could be placed under a vacuum during the mixing process. A commercial H-VAC vacuum pump was used to remove gas bubbles created in the fuel grain during the mixing process. The de-gassed mixture was cast in cardboard sleeves with a 2.67 cm OD polyvinyl chloride (PVC) pipe used as a mandrel. Before casting, the mandrel was coated with Ease Release[®] 400 mold release agent to insure proper release after the fuel grain cured.

Each fuel grain was approximately 57.15 cm in length, 8.26 cm in diameter, the initial fuel port diameter is 2.67 cm, and post combustion chambers are 5.66 cm in diameter and 1.27 cm deep. The mean density of the HTPB fuel grains used for these tests was approximately 966 kg/m³, and the cast fuel grains had a mean mass of 2.50 kg. Fig. 3.7 presents a schematic of the test motor.

Chapter 4

Closed-Loop Throttle Controller Development

Prior to the throttling experiments, the motor configuration described in Chapter 3 was fired multiple times and was found to produce a mean thrust of approximately 786 N with a run-to-run standard deviation of approximately 30 N [39]. Figure 4.1 compares nine motor burn thrust time histories. Even though the motors were constructed identically and the fire control process was computer automated, the run-to-run thrust profiles vary substantially. This variability is inherent to N_2O -HTPB hybrid motor designs and can be caused by a number of factors including oxidizer temperature, ambient pressure, air bubbles in the fuel grain, improper mixing of fuel grain constituents, and nozzle erosion. Motor variability is a primary motivation for the closed-loop throttling methods presented in this paper.

4.1 Evaluation of Chamber Pressure and Thrust as Throttle Control Feedback Measurements

The two most obvious measurement feedback options for a hybrid rocket throttle controller are chamber pressure and thrust. Because both feedback methods are viable options, both were evaluated as part of this project. Either option may be preferable under the conditions in which it is being implemented.

Thrust-feedback is convenient for static testing because a load cell can be attached at the front of the motor. However, in-flight the thrust is measured using the acceleration and rotation rates of the vehicle. Coupling the controller with the vehicle dynamics eliminates the possibility of a stand-alone throttle controller and can make the controller much more complicated in some situations. Additionally, load cell based thrust data tend to be noisy and may feed back unwanted test stand structural harmonics to the control system. The sensed thrust must be significantly filtered and can complicate the overall control imple-

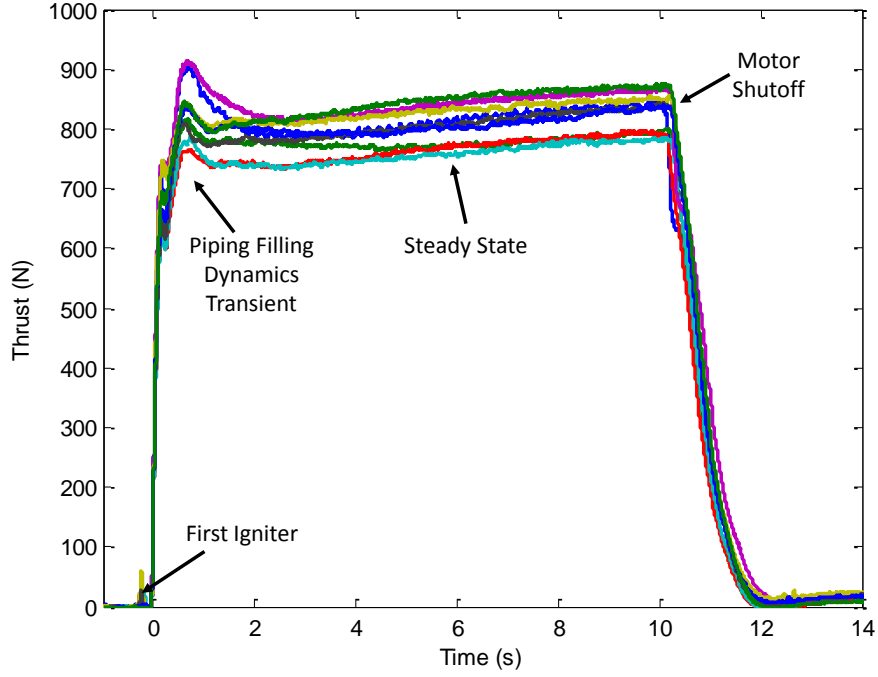


Fig. 4.1: Thrust time histories for previous HTPB motor variability burns.

mentation. While chamber pressure feedback does not provide direct control over thrust, chamber pressure is the strongest driver for motor mass flow and in the absence of o/f shift and nozzle erosion there is a mostly linear relationship.

It should be noted that the motor cap pressure transducer does not measure the true chamber pressure, but rather the pre-combustion chamber pressure, P_{opc} . References to “chamber pressure” in discussions of controller signals and measured values are actually P_{opc} . For a large, circular port the chamber pressure is close in value to P_{opc} , and P_{opc} was consistently used for all controller parameters.

4.2 Control Law Development

Controllers used during this project were either integral (I) or proportional-integral (PI) controllers. Due to the high noise-to-signal ratio during cold-flow testing, a proportional gain could not be used without causing servo jitter. PI controllers were used for both hot-flow feedback mechanisms. Figure 4.2 shows the general structure of the closed-loop

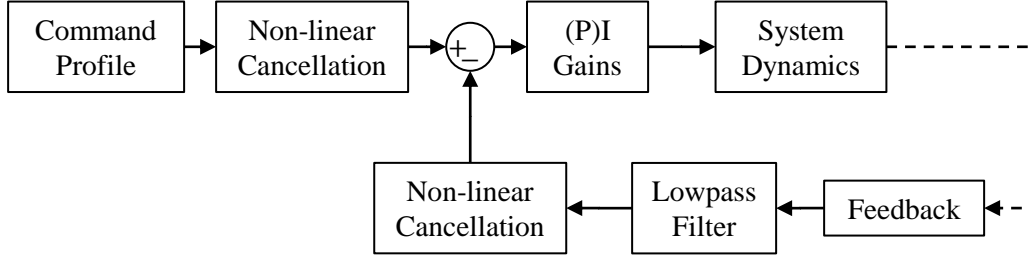


Fig. 4.2: General form of control loop used for closed-loop throttling.

throttling control law.

Although the same control structure was used for all tests, three different operational gain ranges were evaluated for the cold-flow controller and the hot-flow thrust-feedback and chamber pressure-feedback controllers. Motor thrust and chamber pressure require a nonlinear controller to be controlled directly due to the nonlinear relationship between the valve position and its effective port area. In order to simplify the controller, nonlinear cancellation was used to control the thrust or chamber pressure indirectly using the linearly controlled valve position. The relationship between thrust or chamber pressure and valve position was determined experimentally through open-loop testing. This relationship allows valve position to be parametrized as a function of thrust or chamber pressure inputs. Thrust and chamber pressure command and feedback signals were subsequently converted to an estimated valve position and the control loop was closed around the error in valve position. By closing the loop around valve position error, the nonlinearity between the valve position and effective port area was separated from the controller and effectively canceled. Large deviations in motor performance from the motors used during open-loop testing could potentially cause instabilities in the controller through the nonlinear cancellation, but variances in performance of the test motor configuration were not large enough to cause instability.

In the controllers, especially the cold-flow controller, feedback noise was a significant factor in controller stability. A lowpass filter was used to remove higher frequency noise from the feedback signal. Potential high-frequency instabilities are discussed in Section 4.3. All controllers were run at a loop frequency of 100 Hz. The loop frequency was limited by

the processing power of the cFP. Steps taken to reduce processing load of the cFP included limiting data recording to when the control loop was running, building a data array and recording data at completion of the test instead of recording real-time, and limiting the number of global variables.

4.2.1 Cold-Flow Controller

Preliminary closed-loop throttle tests were performed using a top-pressured nitrous oxide cold-gas system. Cold-flow tests were performed first because of their reduced cost and risk. Multiple tests could also be performed in succession without replacing fuel grains and ignitors, making it easier to compare results from multiple gain sets to simulator results. The cold gas system used for cold-flow testing consisted of all of the same MoNSTeR Cart feedline piping used for hybrid motor testing and the motor cap and injector from the 98 mm test motor. Helium top-pressurized nitrous oxide was evacuated through the 3.8 mm orifice in the injector to ambient conditions.

During testing the motor top cap was mounted to the MoNSTeR Cart thrust stand. The 2225 N axial load cell was intended to read much higher thrust and the noise level of the signal was a significant portion of the maximum thrust that the cold gas system could produce. To minimize the effect of the signal noise on controller performance, an integral controller was used. Only step input command profiles were used in the cold-flow controller. Because of the high noise-to-signal ratio, ramp input response would be difficult to discern.

A commanded thrust profile was pre-programmed and used as a tracking signal for the controller. To synchronize the controller VI with the test computer VI, a thrust trigger was built into the controller. When the controller VI was set to “active” mode in the test VI, the throttle valve was programmed to open to an initial position and remain there while the thrust level was below the threshold. At the end of the test the same threshold value was used to signal the controller to stop. A heavily filtered thrust signal was used to avoid controller initiation due to noise spikes. Thrust levels were low enough during cold-flow testing that controller overshoot could cause the thrust level to dip below the threshold and turn off the controller mid-test. To avoid terminating the controller mid-test,

the thrust trigger was set just above the normal noise level and the lower command setting of the controller was high enough to leave a buffer zone. The highest noise level before test initiation was around 5 N, so the thrust trigger was set to 10 N. Lower command thrust levels were set no lower than 30 N to ensure that the threshold value was not reached during the test due to controller overshoot.

Logarithmic functions of the form

$$x = -\ln\left(-\frac{F_t}{A} + 1\right)\tau + x_0 \quad (4.1)$$

were used in the nonlinear cancellation, where x is the valve position in %MVT, F_t is the thrust, and the other variables are experimentally derived curve fit coefficients. Equation (4.1) is the inverse of Eq. (6.5). To ensure that values returned from the functions were real and finite, an upper thrust limit was set to a value just smaller than A . If the measured thrust exceeds the limit, the signal is reset to the limit value.

4.2.2 Thrust-Feedback Hot-Flow Controller

While the thrust-feedback controller was less sensitive to noise than the cold-flow controller, load cell signal noise was still an issue. This load cell noise precluded the inclusion of a derivative term in the control law. Both a step input command thrust profile analogous to a boost/sustain/boost flight profile of a tactical missile and a step-down/ramp-up flight profile analogous to an optimum altitude profile of a sounding rocket were used for thrust-feedback demonstration.

Because both the thrust-feedback controller and the cold flow controller used the same load cell input, much of the same setup was used. The simulator and controller VI required no re-programming, only changes to a few parameter values. Curve fit coefficients used in the nonlinear cancellation were changed to match the higher thrust of the hot-flow system; and, consequently, the upper thrust limit was changed. Reaching the threshold thrust value and terminating the controller mid-test was not as much of a concern as it was for the cold flow controller, so the thrust trigger was set to 20 N to provide a greater buffer from noise

spikes in the load cell signal.

4.2.3 Chamber Pressure-Feedback Hot-Flow Controller

For the chamber pressure-feedback controller an a priori conversion between thrust and chamber pressure was made to loosely provide thrust control. Thrust and chamber pressure have a slightly quadratic relationship in the test motor. The experimentally derived equation that was used to match the chamber pressure command profiles to command profiles used for the thrust-feedback controller,

$$P_0 = \frac{\sqrt{-4a_1c_1 + 4a_1F_t + b_1^2} - b_1}{2a_1}, \quad (4.2)$$

is the inverse of the quadratic equation described in Eq. (5.4).

The signal to noise ratio of the pressure transducer was much lower than for the load cell. A derivative gain could be used for the chamber pressure-feedback controller. However, a PI controller was sufficient to demonstrate the controller and required fewer changes to the controller VI. The same thrust trigger was used to initiate the controller as in the thrust-feedback controller VI. The simulator also required slight modification to model the chamber pressure-feedback controller.

4.3 Hot-Flow System Latencies and Sources

Table 4.1 presents calculated and measured latencies due to servo speed and filling times of the system piping and combustion chamber. These were considered the governing delays in the system and smaller delays such as the oxidizer vaporization delay and the boundary layer combustion delay were assumed negligible. Table 4.1 also presents the sources expected to dominate the throttle controller. A second order Butterworth lowpass filter was used in the controller to prevent unwanted modes feeding into the controller as instrument noise. The following subsections describe these latencies and sources in detail.

Table 4.1: Hot-flow system latencies and sources.

Latency/Source	Approximate Maximum Latency/ Lowest Frequency
servomotor	0.8 s
system piping response	0.14 s
filling dynamics	0.01 s
hybrid low frequency non-acoustic mode	50 Hz
test stand resonant mode	30 Hz
acoustics 1/L mode	350 Hz
Strouhal vortex shedding	350 Hz

4.3.1 Servomotor

Delays in the servo response were due to the maximum servo speed and the settling time of the built-in positioning controller. As provided, the factory preset control gains of the internal PID servo position controller produced a sluggish response that was insufficient for throttling. To speed up valve actuation times, the gains were modified so that the internal position controller was critically damped. Figure 4.3 compares the servo response time for a 10% MVT change in position using the original and the modified gains. Note that the servo response with the original gains was measured using a lower resolution external potentiometer so the apparent steps in the response are measurement artifacts and do not reflect the actual response.

With the modified gains, the time constant for valve repositioning was 0.2 seconds and maximum travel speed was 60% MVT per second. For the range of valve positions required for this project, the maximum delay due to the servo was estimated to be 0.8 seconds.

4.3.2 Pneumatic and Hydraulic Response of the System Piping

The system piping fill delay is calculated by [47]

$$\tau_p = K \frac{V_p \rho_g}{\dot{m}_i} \frac{(\bar{P}_i - \bar{P}_c)}{2\bar{P}_i}, \quad (4.3)$$

where V_p is the system piping volume, ρ_g is the density of the gas phase of the fluid in the system piping, \dot{m}_i is the mass flow rate through the injector, \bar{P}_i is the average injector manifold pressure, \bar{P}_c is the average combustion chamber pressure, and the total compressibility

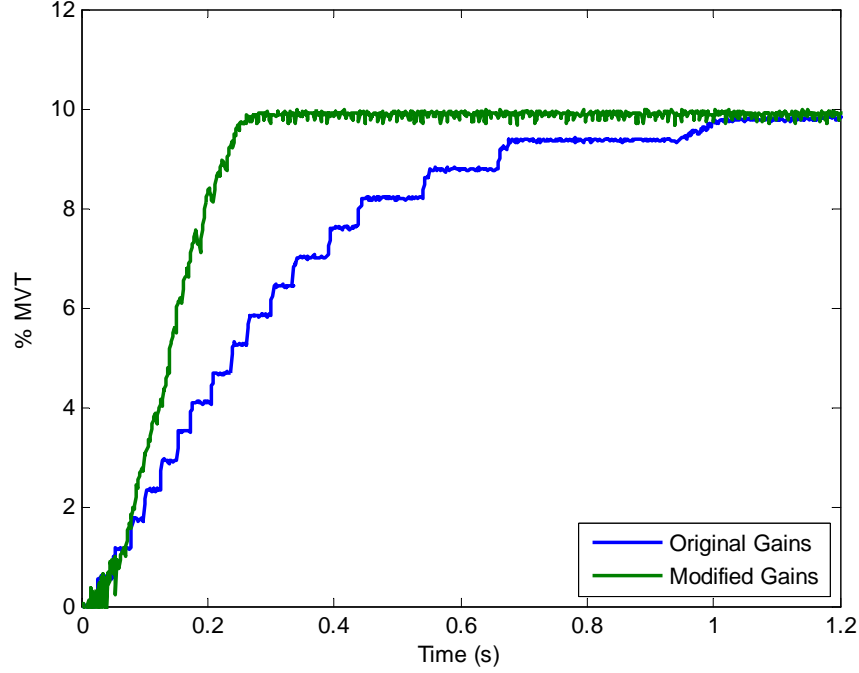


Fig. 4.3: Servo response time with original and modified gains.

parameter, K , is

$$K = \frac{[X_{ox}/\gamma_{ox} + \beta_s \bar{P} (\rho_g/\rho_l) - \bar{P} (\partial X_{ox}/\partial \bar{P})_s]}{[X_{ox} + \rho_g/\rho_l]^2}, \quad (4.4)$$

where X_{ox} is the quality of the oxidizer, γ_{ox} is the oxidizer ratio of specific heats, ρ_l is the liquid phase density of the oxidizer, and \bar{P} is the average pressure in the system piping. Because a single port injector was used for this project, there was no injector manifold and the same values were used for \bar{P} and \bar{P}_i . The liquid compressibility factor, β_s , is the inverse of the bulk modulus of the oxidizer, defined as [48]

$$M_B = \frac{P_2 - P_1}{1 - \rho_1/\rho_2}, \quad (4.5)$$

which describes the difference in the amount that a substance compresses between two different pressures, P_1 and P_2 ; ρ_1 and ρ_2 are the densities corresponding to those pressures. The bulk modulus has a nearly linear relationship with temperature. Using temperatures and pressures in the ranges expected in the oxidizer feed line, a linear function of temperature

was developed to approximate M_B .

Two-phase thermodynamic properties were determined using a Helmholtz model [49–51]. Measured temperatures, pressures, and mass flow rates were assumed to be representative of the average values in the system piping. The calculated values of τ_p ranged between 0.02 and 0.14 seconds for the full throttling range.

4.3.3 Combustion Chamber Filling Dynamics

The combustion chamber fill time is given by [47]

$$\tau_c = \frac{f_c(\gamma)}{C_{dn}} \frac{RT_c}{R\bar{T}} \frac{L^*}{c^*}, \quad (4.6)$$

where C_{dn} is the nozzle discharge coefficient, RT_c is the product of the gas constant and combustion temperature at the nozzle entrance, $R\bar{T}$ is the product of the average gas constant and temperature in the combustion chamber, L^* is the ratio of the chamber volume to the nozzle throat area, c^* is the characteristic velocity, and

$$f_c(\gamma) = \frac{\eta_c}{\gamma} \left(\frac{\gamma + 1}{2} \right)^{(\gamma+1)/(\gamma-1)} \quad (4.7)$$

where η_c is the combustion efficiency and γ is the ratio of specific heats of the combustion products. Combustion properties c^* , T_c , \bar{T} , γ , and the average and nozzle molecular weights were calculated using NASA’s Chemical Equilibrium with Applications (CEA) program [52, 53]. The nozzle discharge coefficient was estimated to be 0.98 [44]. Previous testing showed the combustion efficiency to be about 0.97 for this motor configuration [39]. The calculated combustion chamber fill time was 0.01 seconds.

4.3.4 Low Frequency, Non-Acoustical Pressure Oscillations (Hybrid Low Frequency Mode)

The frequency value of the hybrid low frequency mode is calculated using [54]

$$f_l = 0.234 \left(2 + \frac{1}{o/f} \right) \frac{4}{\pi} \frac{\dot{m}_{ox} R \bar{T}}{L_f P_0 d_p^2}, \quad (4.8)$$

where \dot{m}_{ox} is the oxidizer mass flow rate, L_f is the fuel grain length, P_0 is the chamber pressure, and d_p is the fuel port diameter. Oxidizer mass flow rate and chamber pressure were estimated from experimental data. The lowest calculated frequencies occur near the end of the burn when the o/f is about 6 and the average port diameter is about 5 cm. The calculated values of the hybrid low frequency mode occurs between about 50 and 200 Hz.

4.3.5 Test Stand Resonance

The test resonant frequency was determined by delivering an impulse to the thrust stand and measuring the frequency response in the load cell. A Fourier transform of the load cell noise with and without the impulse is shown in Fig. 4.4. The peak of the lowest resonant frequency is at approximately 30 Hz. The noise spike that occurs in both signals in Fig. 4.4 is unidentified, but is likely radio frequency interference being picked by the load cell. This noise is removed by the lowpass filter in the controller.

4.3.6 Motor Internal Primary Acoustic Mode

Hybrid rocket motor first longitudinal acoustic modes are calculated as [54]

$$f_a = \frac{\sqrt{\gamma R \bar{T}}}{2L_c}, \quad (4.9)$$

is the average speed of sound in the chamber and L_c is the combustion chamber length. The lowest acoustical mode frequency was calculated to be 350 Hz.

4.3.7 Vortex Shedding

The Strouhal number is defined as [54]

$$\text{Sr} = \frac{f_{vs} l}{U}, \quad (4.10)$$

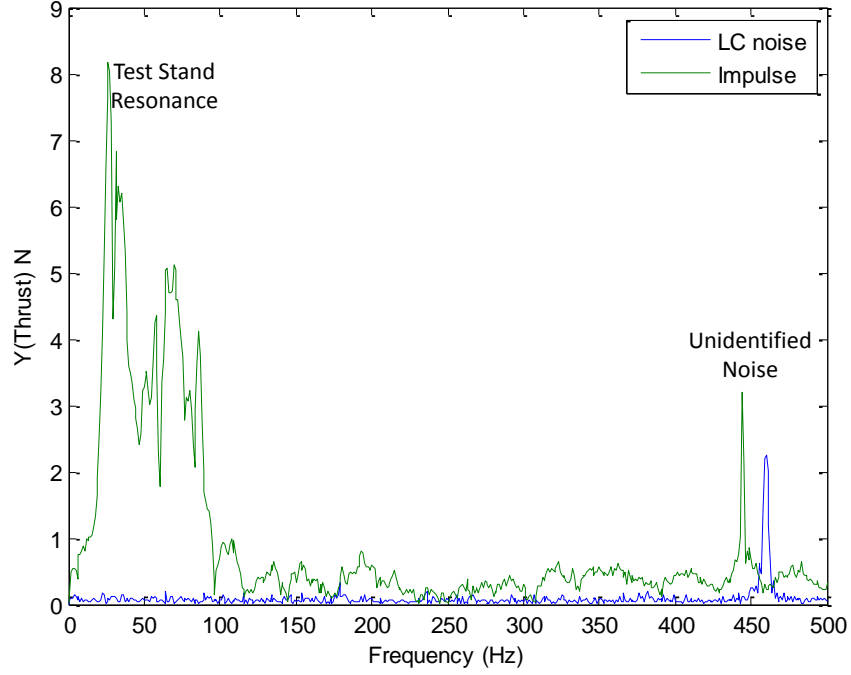


Fig. 4.4: Test stand frequency response to applied impulse.

where f_{vs} is a vortex shedding frequency, l is the characteristic length, and U is the fluid velocity. The vortex shedding frequency is calculated by rearranging Eq. (4.10) to solve for f_{vs} . In hybrid rocket motors, Sr ranges between 0.25 and 0.5. For the throttling valve, the characteristic length was assumed to be the fully-open port diameter. The fluid velocity is calculated as

$$U_v = \frac{\dot{m}_{ox}}{\rho_{ox} A_v}, \quad (4.11)$$

where ρ_{ox} is the oxidizer density and A_v is the valve port area. At the valve, the lowest vortex shedding frequency is about 550 Hz. At the aft end of the fuel grain the fluid velocity is calculated as

$$U_f = \frac{4}{\pi} \frac{\dot{m}_{tot}}{d_p^2} \frac{RT}{P_0}, \quad (4.12)$$

where \dot{m}_{tot} is the total mass flow rate of fluid at the fuel grain exit. The product of the gas constant and temperature at the fuel grain exit was assumed to be approximately equal to

$R\bar{T}$ and l was assumed to be the exit diameter of the fuel grain. Based on these parameters Eq. (4.12) calculates that the lowest vortex shedding frequency at the fuel grain exit occurs at approximately 350 Hz.

Chapter 5

End-to-End System Simulation

Because a PID-type controller was used for throttle the controller, an analytical means for predicting gains would be difficult to produce. Instead, a simulator was created to provide an immediate prediction of system behavior for gain tuning and to predict controller behavior. Using a simulator to predict the controller response for various settings allowed for the controller to be set up without extraneous system classification testing. The throttling system simulator was developed using MATLAB and Simulink. The Simulink model is shown in Fig. 5.1. An accompanying driver code was written in MATLAB. Individual modules within the simulator are highlighted in Fig. 5.1 and numbered as 1) proportional-integral-derivative (PID) controller gains, 2) system piping feed physics, 3) servo, and 4) instrument noise. These modules are described in detail in the following sections.

5.1 PID Controller Gain Model

A PID controller was used in the simulator so that the derivative gain, K_D , could be modeled [55]. As mentioned in Section 4.2, the test controllers used either proportional and integral gains, K_P and K_I , or only K_I , but the capacity to model K_D was built in so that no changes to the simulator would be required if a PID controller is used for future projects. A discrete-time trapezoidal integrator was used for the integral gain to match the integrator used in the test controllers. Figure 5.2 shows the PID controller used in the simulator.

The PID controller gains were originally modeled based on the LabVIEW PID controller block to provide better agreement between the simulator and the controller VI [56]. Later, the LabVIEW PID block was abandoned to provide greater flexibility and the gains were converted to standard format, but the LabVIEW signal flow path remained. Figure 5.3 shows how the gain model was integrated into the simulator control loop.

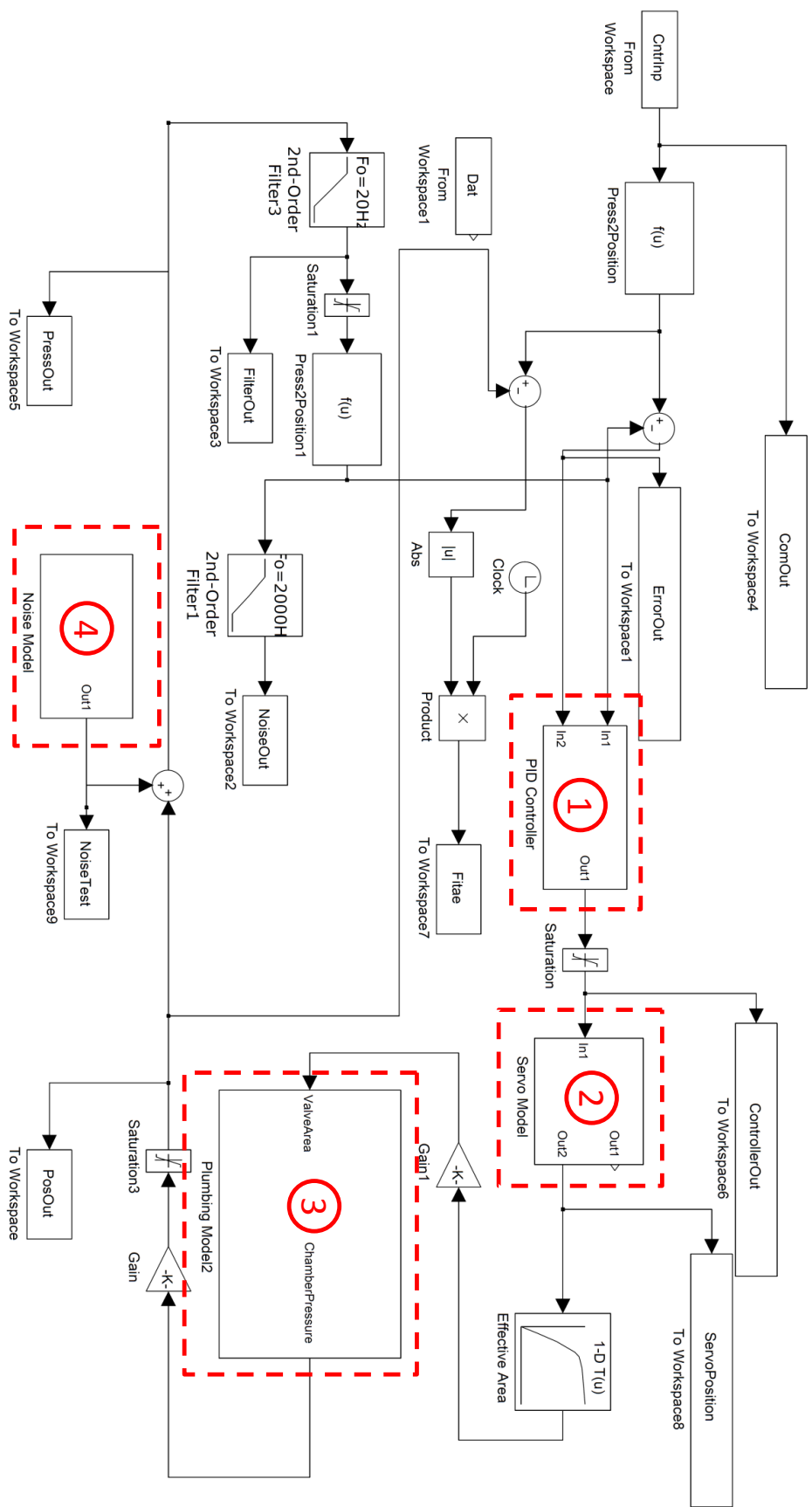


Fig. 5.1: Simulink throttling system model.

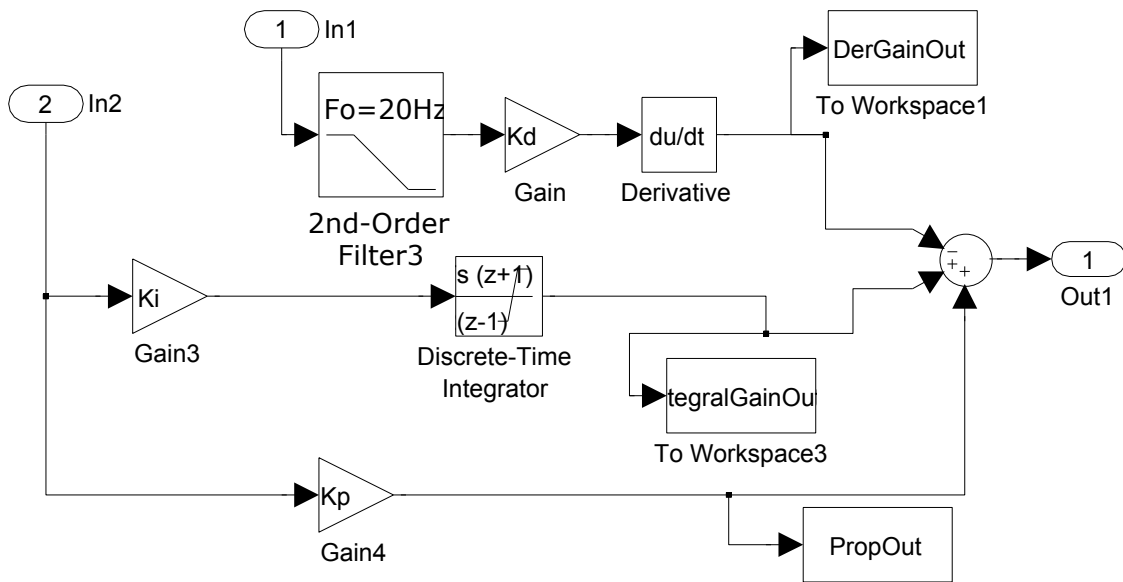


Fig. 5.2: Simulink PID controller.

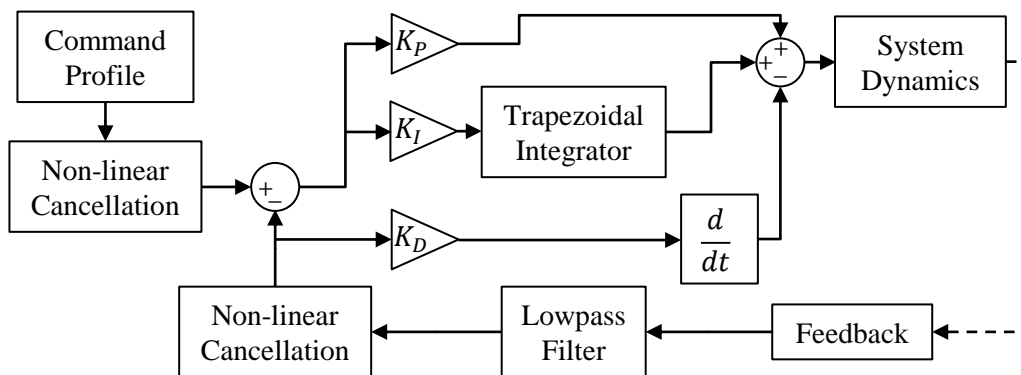


Fig. 5.3: Simulator control loop with expanded gain section.

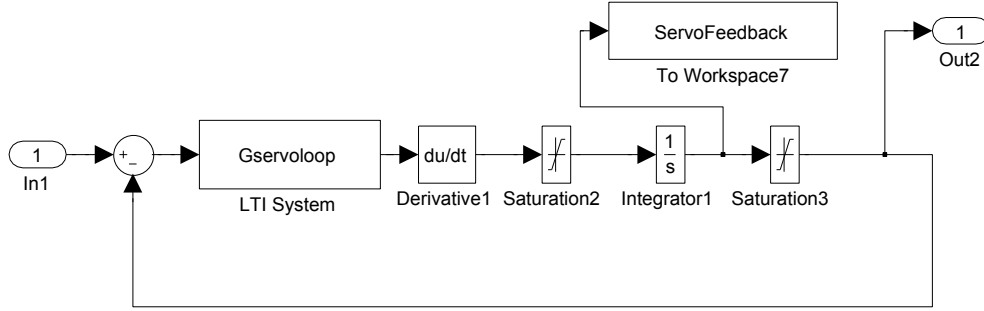


Fig. 5.4: Simulator servo model.

5.2 Servo Model

Rather than modeling the individual latencies discussed in Section 4.3, an empirically derived transfer function was used to model the total delay in the thrust or chamber pressure response to changes in valve position. The assumed form of the transfer function is

$$G(s) = \frac{1}{\tau_1 \tau_2 s^2 + s(\tau_1 + \tau_2)}, \quad (5.1)$$

where τ_1 and τ_2 are time constants acquired during open-loop testing as outlined in Section 6.3 below. The maximum servo speed was modeled by saturating the rate of change in the servo position. Figure 5.4 shows the simulator servo model.

5.3 Oxidizer Feed Systems Response Model

Figure 5.5 shows the basic algorithm used to model the system piping feed physics. Two phase oxidizer flow through the throttle valve and the injector was modeled using the non-homogeneous, non-equilibrium (NHNE) model of Dyer et al [57]. Nitrous oxide properties were calculated using a Helmholtz equation of state as presented by Span and Wagner [49–51]. Figure 5.6 shows the thermodynamic properties used for each oxidizer state in the oxidizer feed system model. Conditions were assumed to be isenthalpic (constant enthalpy) between states and isentropic (constant entropy) between a state and the downstream orifice. Shading in the figure refers to the reduction in oxidizer quality as the fluid passes through the control valve and injector orifices.

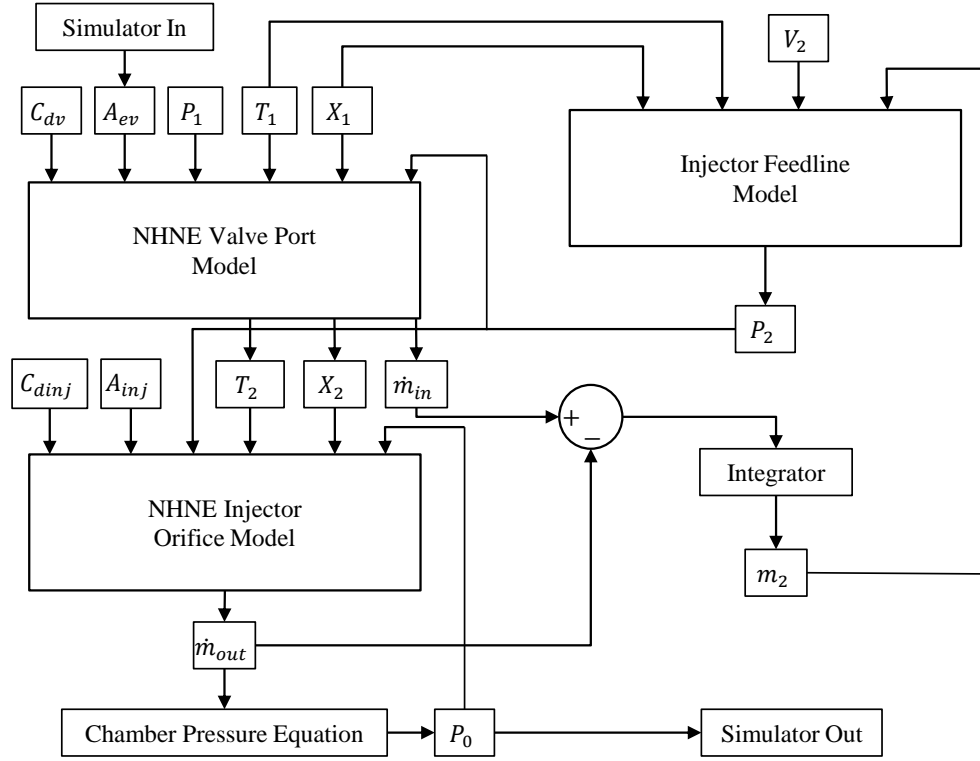


Fig. 5.5: Oxidizer feed system response model.

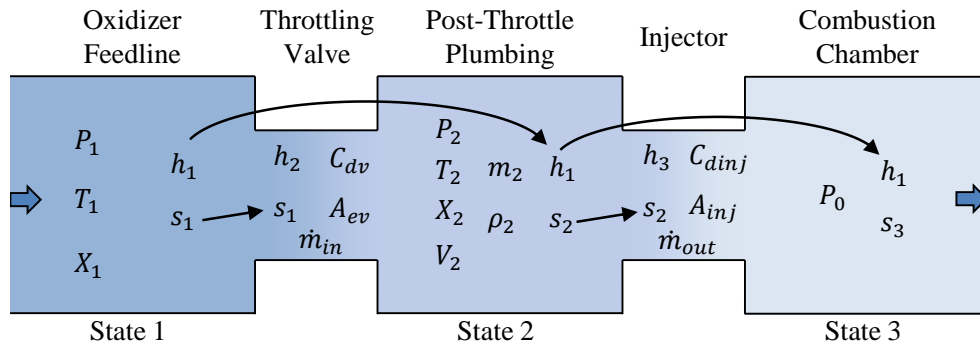


Fig. 5.6: Thermodynamic properties used in system piping feed physics model.

Table 5.1: Constants used in oxidizer feed system response model.

Parameter	Symbol	Value
valve discharge coefficient	C_{dv}	0.7
oxidizer feedline pressure	P_1	5500 kPa
oxidizer feedline temperature	T_1	294 K
oxidizer feedline quality	X_1	1
post-throttle system piping volume	V_2	$6.32 \times 10^{-5} \text{ m}^3$
injector discharge coefficient	C_{dij}	0.7
injector orifice area	A_{inj}	$1.14 \times 10^{-5} \text{ m}^2$

Before the system piping model, the servo position signal is transformed to effective valve port area using a table look up. Effective valve port areas were calculated by solving for the area required for the system piping model output to match experimental chamber pressure data at various valve positions, assuming a constant discharge coefficient. Chamber pressure was used to calculate the effective valve area because it was needed in both the thrust and the chamber pressure-feedback simulators.

Because the oxidizer system is regulated by a top pressurant, oxidizer conditions upstream of the throttle valve do not vary greatly between tests. Because the conditions remain relatively unchanged, representative values averaged from experimental data were used for the first state. These average values were used in the NHNE model to compute the mass flow rate (\dot{m}_{in}) as a function of P_1 , s_1 , and P_2 through the valve port and the conditions at State 2. Table 5.1 presents these constant values, as well as others used in the system piping model.

The pressure at State 2 was computed using the Helmholtz equation of state and a Newton-Raphson solver [58]. Temperature and density are required to determine state properties using the Helmholtz equation. Density, ρ_2 , was determined by integrating the net mass flow rate into the post-throttle system piping to find the mass, or

$$m_2 = \int \dot{m}_{in} - \dot{m}_{out}, \quad (5.2)$$

and dividing it by the internal volume of the post-throttle system piping, V_2 . Temperature was determined using the Newton solver to match the enthalpies of State 1 and State 2.

The pressure in the post-throttle system piping is calculated as the saturation pressure with the density in the system piping and at the temperature at which the isenthalpic condition is satisfied.

Conditions computed by the first NHNE model and the post-throttle system piping pressure were used in a second NHNE model to compute the mass flow rate through the injector (\dot{m}_{in}) as a function of P_2 , s_2 , and P_0 . Chamber pressure has an approximately linear relationship with injector mass flow rate in the test motor configuration. Experimental data was used to produce the equation,

$$P_0 = a_2 \dot{m}_{out} + b_2, \quad (5.3)$$

that calculates chamber pressure based on \dot{m}_{out} , where a_2 and b_2 are experimentally derived curve fit coefficients described further in Section 6.4. For the pressure-feedback controller model, this chamber pressure value was output to the simulator.

For the thrust-feedback controller, another experimentally derived equation described in Section 6.4 was used to calculate thrust based on the chamber pressure. Thrust had a slightly quadratic relationship with chamber pressure in the test motor configuration. The equation used to compute thrust is

$$F_t = a_1 P_0^2 + b_1 P_0 + c_1. \quad (5.4)$$

When the full system piping model was placed in the simulator run times became excessive. In order to decrease simulator run times, data from the full system piping model was used to make look up table blocks so that the imbedded MATLAB functions could be bypassed. The look up table version of the system piping model is shown in Fig. 5.7.

5.4 Measurement Feedback Noise Model

Figure 5.8 shows the Simulink noise model for the feedback pressure signal. Instrument noise was modeled in Simulink by matching the dominant frequency modes in the noise. The

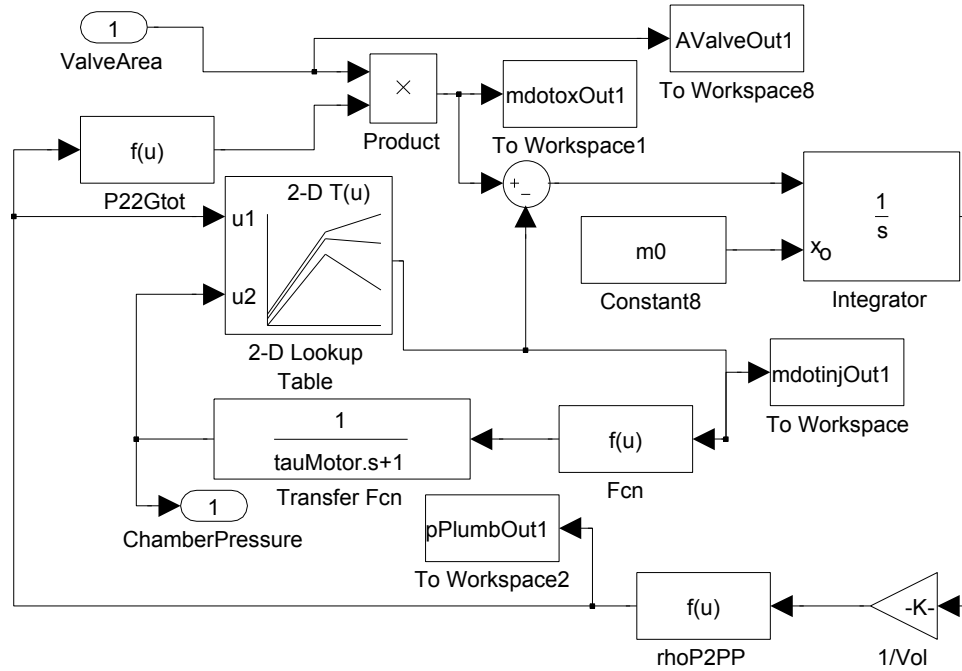


Fig. 5.7: Simulator system piping model with look up tables.

Simulink Band-Limited White Noise block defines the noise power input as the height of the power spectral density (PSD) of the white noise. The amplitude of the frequency modes were matched by plotting the PSD of the actual noise and adjusting the noise power level in each Band-Limited White Noise block until the amplitudes matched. A Bandpass Filter block was used to adjust the bandwidth of each mode to match those in the instrument PSD. Figure 5.9 shows the PSD of the actual and simulated noise for the pressure transducer.

5.5 Gain Tuning

Gains were tuned in the simulator by sweeping through a wide range of gains and plotting the results. Figure 5.10 shows the results from a simulator run using a step command input with a chamber pressure-feedback controller. In the plots, the green trace is the command input and the blue and red, respectively, are the raw and filtered response. The proportional gain was varied between 0.2 and 0.5 by steps of 0.1 and the integral gain was varied between 1.5 and 3.5 by steps of 0.5. A wider range with larger step sizes was used initially to determine a range of effective gains and then a finer sweep was made through

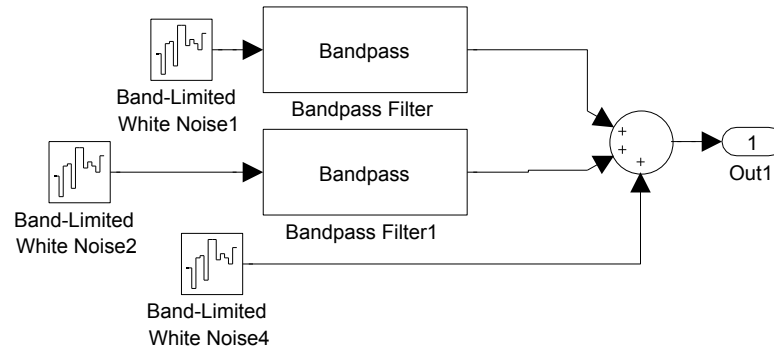


Fig. 5.8: Pressure transducer noise model.

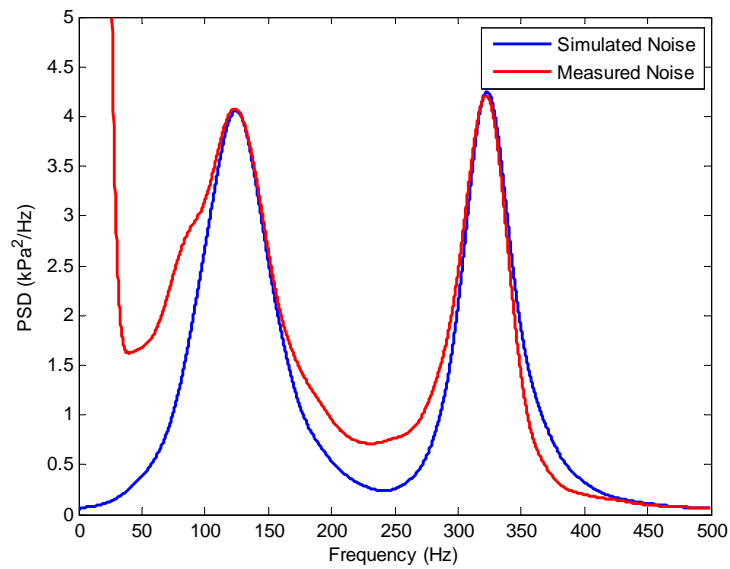


Fig. 5.9: PSD of simulated and real pressure transducer noise.

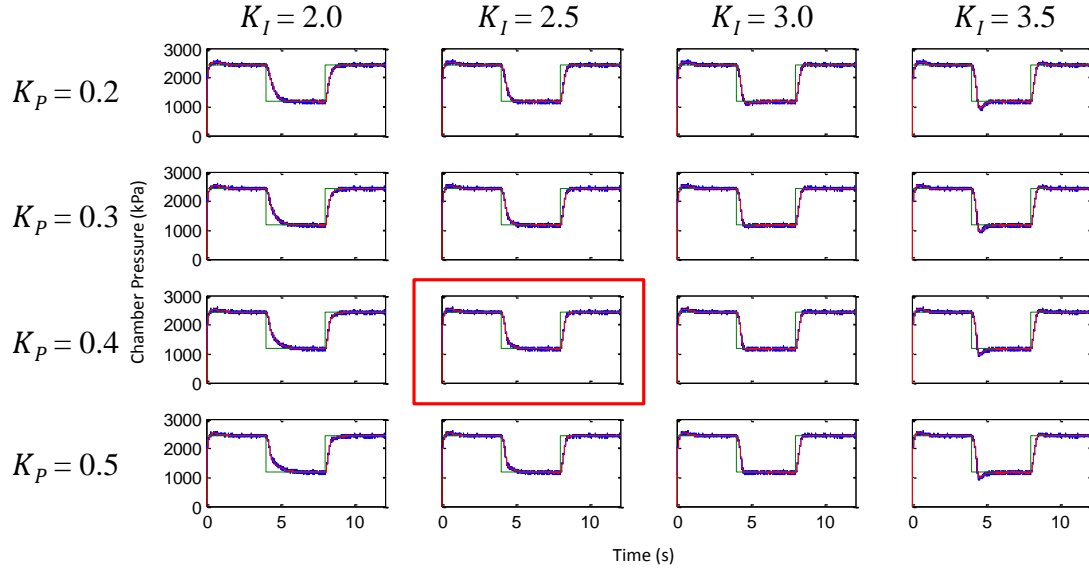


Fig. 5.10: Plots of controller response to a range of gains.

that gain range to pick final gain values.

To provide a means of comparison between simulator runs, controller performance was rated using the integral of the absolute magnitude of the error times the run time (ITAE), calculated as [55]

$$\text{ITAE} = \int_0^{t_{\text{tot}}} |te(t)| dt, \quad (5.5)$$

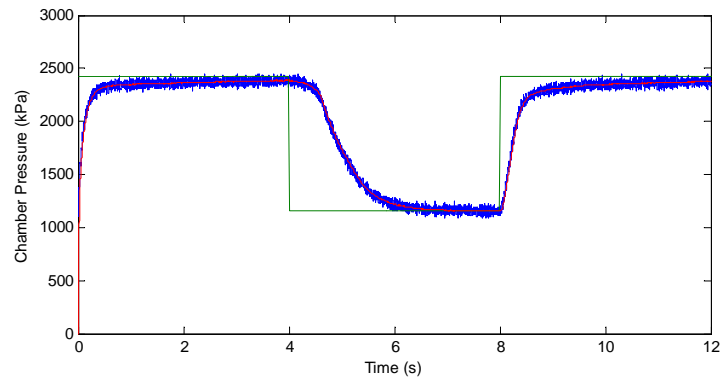
where t is the run time, $e(t)$ is controller error as a function of run time, and t_{tot} is the total simulator run duration. Several methods exist to rate the performance of a controller. Normally, a method is selected to emphasize a particular controller response characteristic such as steady-state accuracy or settling time. Because the goal of this project is to prove a concept and there is no particular application, no specific characteristics needed to be emphasized and ITAE was chosen randomly. Table 5.2 presents ITAE values corresponding to the plots in Fig. 5.10. The plot of the simulator run with gain values chosen for some of the chamber pressure feedback tests is boxed in Fig. 5.10. Due to a slight discrepancy between simulator and test results, the chosen gains were reduced by a single step from those predicted to give the lowest ITAE score.

When a set of gains was selected it was checked to verify that it would work if motor

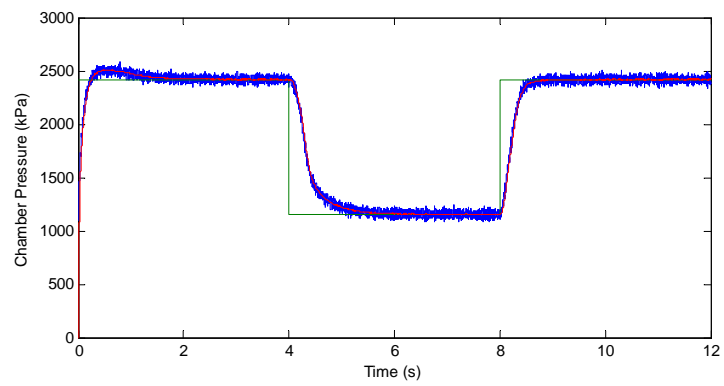
Table 5.2: ITAE ($\text{kPa}\cdot\text{s}^2$) values corresponding to plots in Fig. 5.10.

	$K_I = 2.0$	$K_I = 2.5$	$K_I = 3.0$	$K_I = 3.5$
$K_P = 0.2$	5710	4519	4154	4443
$K_P = 0.3$	5738	4477	4001	4356
$K_P = 0.4$	5763	4493	3898	4324
$K_P = 0.5$	5776	4503	3859	4306

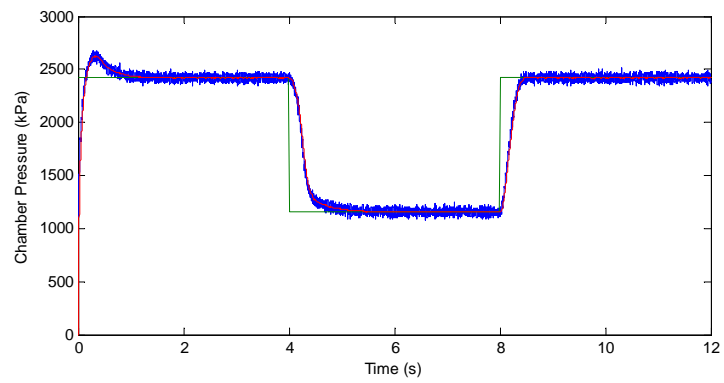
performance varied from the moderate performance parameters that were used for nonlinear cancellation in the controller and for the system piping model in the simulator. Motor variability was modeled by applying a scaling factor to the effective valve port area that was input into the system piping model. The scaling factor was applied as a gain following the table look up for valve effective area, shown in Fig. 5.1. Mean motor thrust and chamber pressure 95% confidence intervals were approximately $\pm 9\%$ for the variability tests performed on the 98 mm motor configuration. This variability was modeled by scaling to $\pm 15\%$ of the effective valve port area, which creates a $\pm 9\%$ variance in the thrust and chamber pressure. Figure 5.11 shows nominal simulator results compared to results from 85% and 115% scaling. Comparison of Figures 5.10 and 5.11 shows that motor variability has a similar effect on the controller to varying the integral gain.



(a) Scale factor = 0.85.



(b) Scale factor = 1.00.



(c) Scale factor = 1.15.

Fig. 5.11: Controller response for three different scaled valve areas.

Chapter 6

Open-Loop Throttle Testing

6.1 Open-Loop Cold-Flow Testing

Open-loop testing was performed to assess system flow dynamics and to establish a baseline for the control valve effectiveness. Performing a cold-flow-only open-loop throttle test decouples the dynamics of the oxidizer delivery system from the more complex dynamics associated with the hybrid rocket motor. During cold-flow testing, nitrous oxide was evacuated through a 3.8 mm orifice into ambient conditions using the apparatus described in Section 4.2. Figure 6.1 shows the thrust produced during a cold-flow test. During this test the throttling valve started at a closed position and was opened 10% MVT every two seconds until it was completely open. Plotted points show times when the step input signal was changed. Results showed that most of the valve's control authority lies within the 30-70% MVT range. As a result, controlled throttling was performed mostly within this range.

6.2 Open-Loop Hot-Flow Testing

Three hot-fire open-loop throttle tests were performed. Results for thrust and chamber pressure are shown in Fig. 6.2. During the first test the throttle valve was not adjusted and was simply left completely open throughout the duration of the burn. For the second test the throttling valve started at 90% MVT and closed in steps of 5% MVT every second. By the end of the burn the valve was in the 50% MVT open position. The third test was conducted at the lower end of throttleability. The valve began at the 65% MVT position and was again closed 5% MVT every second until finishing at the 25% MVT position.

Because the 50-90% MVT throttled test was partially in the region shown to have little control authority by the cold flow tests, the first valve changes had little throttling effect.

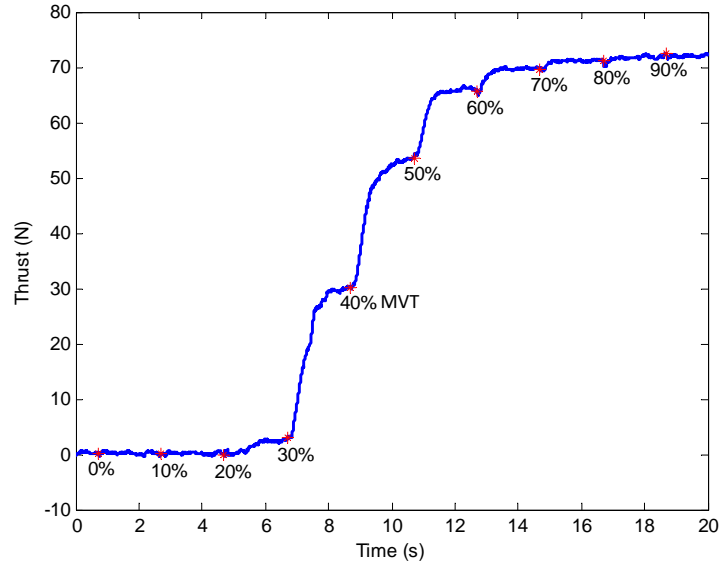


Fig. 6.1: Thrust during cold-flow open loop throttle test.

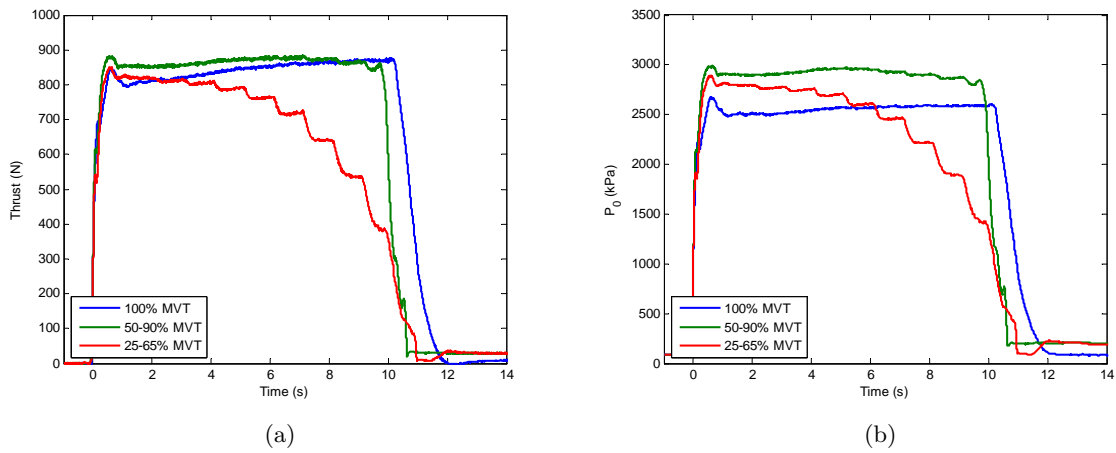


Fig. 6.2: (a) Thrust and (b) chamber pressure during hot flow open loop throttle tests.

As the valve travel entered the region of more control authority, throttling had the effect of leveling off the increase in thrust and chamber pressure and at the end of the burn distinct steps are finally discernible. The 25-65% MVT test began in the region of high control authority. Steps are plainly visible throughout most of the burn duration. The steps do not level off as they do during cold-flow testing because of the gradual increase in thrust and chamber pressure during the burn.

Also, as mentioned previously, N₂O-HTPB hybrid motors have a fairly high degree of run-to-run variability. This variability accounts for the initial peak thrust of the fully-open test being lower than the tests that were partially throttled. The fully-open test demonstrated that the test motors' thrust and chamber pressure increase during the burn.

6.3 Thrust and Chamber Pressure Response Time Constants

The system thrust response time constant was measured to model system latencies in the simulator. Changes in thrust due to step changes in the throttle valve position were normalized to a 0-1 range using the normalizing relationship

$$F_{tn}(t) = \frac{F_t(t) - F_{ti}}{F_{tf} - F_{ti}}, \quad (6.1)$$

where F_{ti} is the measured thrust before the step input, F_{tf} is the measured thrust after settling occurs, and $F_t(t)$ is the measured thrust at any time during the response. Second order nonlinear least squares curve fits of the form

$$y(t) = \frac{1}{\omega_n^2} \left[1 - \frac{1}{\tau_2 - \tau_1} \left(\tau_2 e^{-t/\tau_2} - \tau_1 e^{-t/\tau_1} \right) \right] \quad (6.2)$$

were applied to the normalized thrust curves to obtain step input thrust response time constants τ_1 and τ_2 and the natural frequency ω_n from the time response $y(t)$. Depending on the control law used, $y(t)$ is either the normalized thrust or pressure response of the system. Figure 6.3 shows typical normalized thrust response curves for both cold-flow and hot-flow tests with the throttling valve traveling through the 35-50% MVT range. For

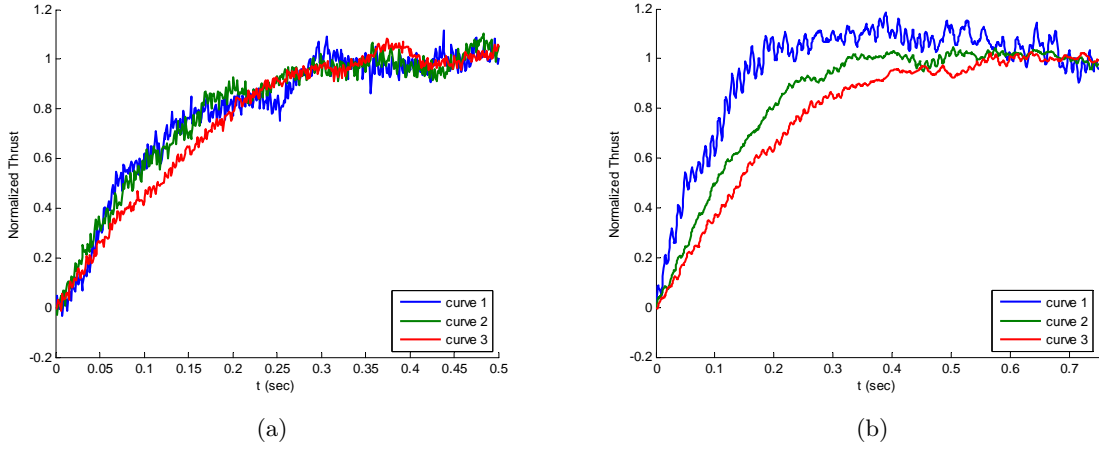


Fig. 6.3: Normalized thrust response curves for (a) cold-flow throttling and (b) hot-flow throttling.

the durations tested, cold-flow thrust can be thought of as primarily a function of valve position and average time constants can be used. During the hot-flow tests thrust drifts over time. However, time constant accuracy proved to have little effect on the simulator for the changes in valve position and thrust durations used for this research. The time variance in the hot-flow step response time constants were ignored and average values $\tau_1 = 0.0221$ s and $\tau_2 = 0.0217$ s were used for both cold-flow and hot-flow simulation. Time constants were the same for thrust and chamber pressure, so the same values were used in both simulator models. The natural frequency was calculated as part of the curve fit, but was not used in the simulator.

6.4 Thrust, Chamber Pressure, and Mass Flow Rate Calibrations

The controllers and simulator requires several computationally efficient conversions between thrust, chamber pressure, and oxidizer mass flow rate. Expressions used for conversions were obtained from curve fits of the open-loop test data shown in Fig. 6.2. Thrust and chamber pressure have a slightly quadratic relationship. A nonlinear least squares curve fit of the form

$$F_t = a_1 P_0^2 + b_1 P_0 + c_1 \quad (6.3)$$

Table 6.1: Curve fit coefficients for thrust, chamber pressure, and mass flow rate calibrations.

Coefficient	Value
a_1	9.21×10^{-6}
b_1	0.28
c_1	-40.15
a_2	8602.47
b_2	152.02

was used to describe the relationship between thrust (N) and absolute chamber pressure (kPa). The relationship between chamber pressure and oxidizer mass flow rate is mostly linear. A linear curve fit of the form

$$P_0 = a_2 \dot{m}_{ox} + b_2 \quad (6.4)$$

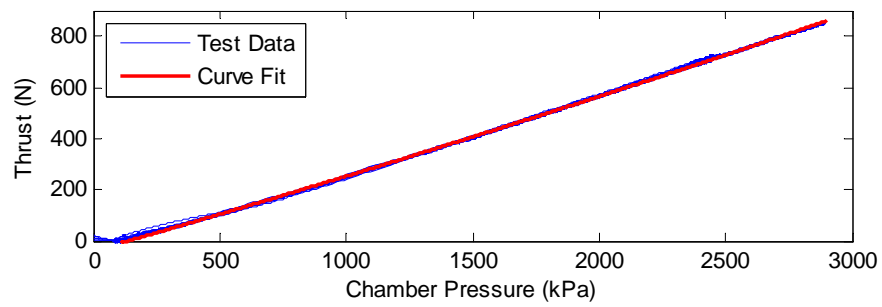
was used to describe the relationship between absolute chamber pressure (kPa) and mass flow rate (kg/s). Thrust can be related to mass flow rate by combining both relationships. Table 6.1 presents the values of the curve fit coefficients used in Equations (6.3) and (6.4). Figure 6.4 shows the curve fit data compared to experimental data. The experimental data shown in Fig. 6.4a was collected from all of the hot-fire open-loop tests performed. While o/f shift occurred during each motor burn, it was not a significant factor in the relationship between thrust and chamber pressure.

6.5 Thrust and Pressure Curve Fits

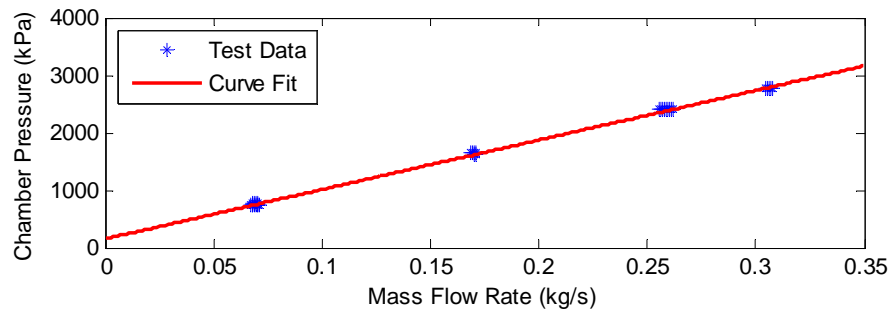
Curve fit data required for use for nonlinear cancellation in the controllers was obtained during open-loop testing. Figure 6.5 shows nonlinear least squares curve fits of thrust and chamber pressure as functions of throttle valve position. Exponential response functions of the form

$$S = Ae^{-(x+x_0)/\tau} + A \quad (6.5)$$

were used for the curve fits, where S is the controller input signal (thrust or absolute chamber pressure), x is the valve position in %MVT, and the other variables are exponential curve fit

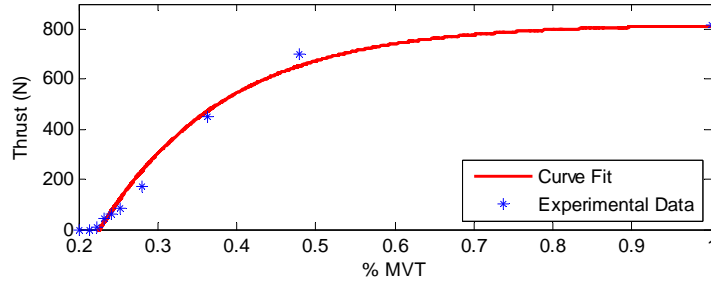


(a)

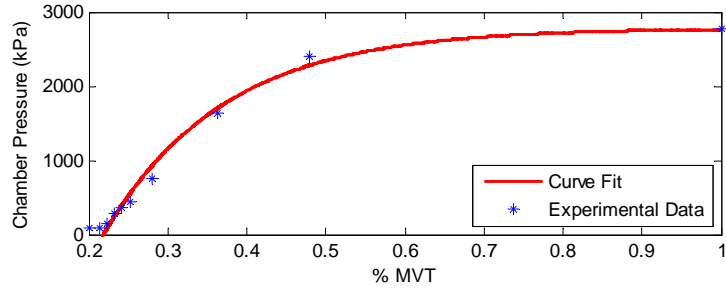


(b)

Fig. 6.4: Chamber pressure, thrust and mass flow calibrations compared to experimentally measured values.



(a)



(b)

Fig. 6.5: Experimentally derived curve fits for (a) thrust and (b) chamber pressure as a function of % MVT.

Table 6.2: Exponential curve fit coefficients used in controllers.

Controller	A	x_0	τ
Cold-Flow	75.04	-0.2527	0.2116
Thrust	819.1	-0.2268	0.1586
Chamber Pressure	2781	-0.2185	0.1522

coefficients that represent scaling (A), initial offset (x_0), and time constant (τ). Equation 6.5 was rearranged into Eq. (4.1) for use in the controllers. Values of the curve fit coefficients used for each controller are displayed in Table 6.2.

6.6 Servo Deadband Evaluation

A deadband was built into the servo position controller by the manufacturer to prevent overheating of the components due to high frequency servo jitter. The deadband limits were measured by commanding a sawtooth wave input and comparing the response of the servo. Figure 6.6 shows input signal voltage and servo position response plots that have been normalized by their respective maximum values for a more convenient visual representation

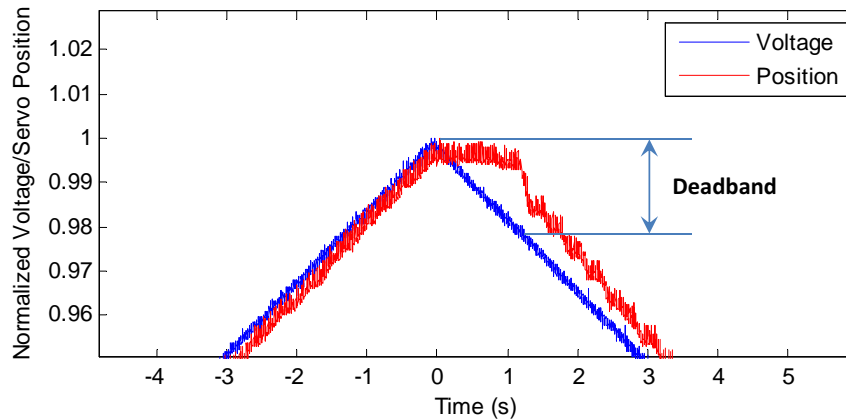


Fig. 6.6: Results for a servo deadband test.

of the deadband (note that the normalized values are used for illustration only and were not used to compute the deadband). The measured deadband was ± 0.02 volts or $\pm 1.25\%$ of the total travel. Effects of the deadband on the throttle controllers included a lack of response fidelity while at a constant set point, a small step at the beginning of ramp input profiles, and a slight delay in response to a ramp input. Although the controller was affected by the servo deadband, the deadband was left in place to avoid damage to internal servo components.

6.7 Deep Throttling Hot-Flow Testing

An open-loop deep throttle test was performed in order to demonstrate the limits of motor throttling. Combustion remained stable with throttling ratios as high as 66:1. Figure 6.7 shows a thrust time history for the deep throttle test with images corresponding to several of the thrust set points during the test. The numbers displayed in the images are the percentage of peak thrust and a time stamp corresponding to the time axis of the plot. Combustion became unstable at point (5) in Fig. 6.7. Figure 6.8 shows a more detailed plot of the unstable region with thrust and chamber pressure normalized by the peak values.

As a point of comparison, the Space Shuttle Main Engine (SSME) was normally throttled within a ratio of 1.67:1, but was demonstrated as high as 5.88:1 [59]. Deep throttling is defined as having a turndown ratio higher than 4:1 for a liquid engine. A 2010 deep throt-

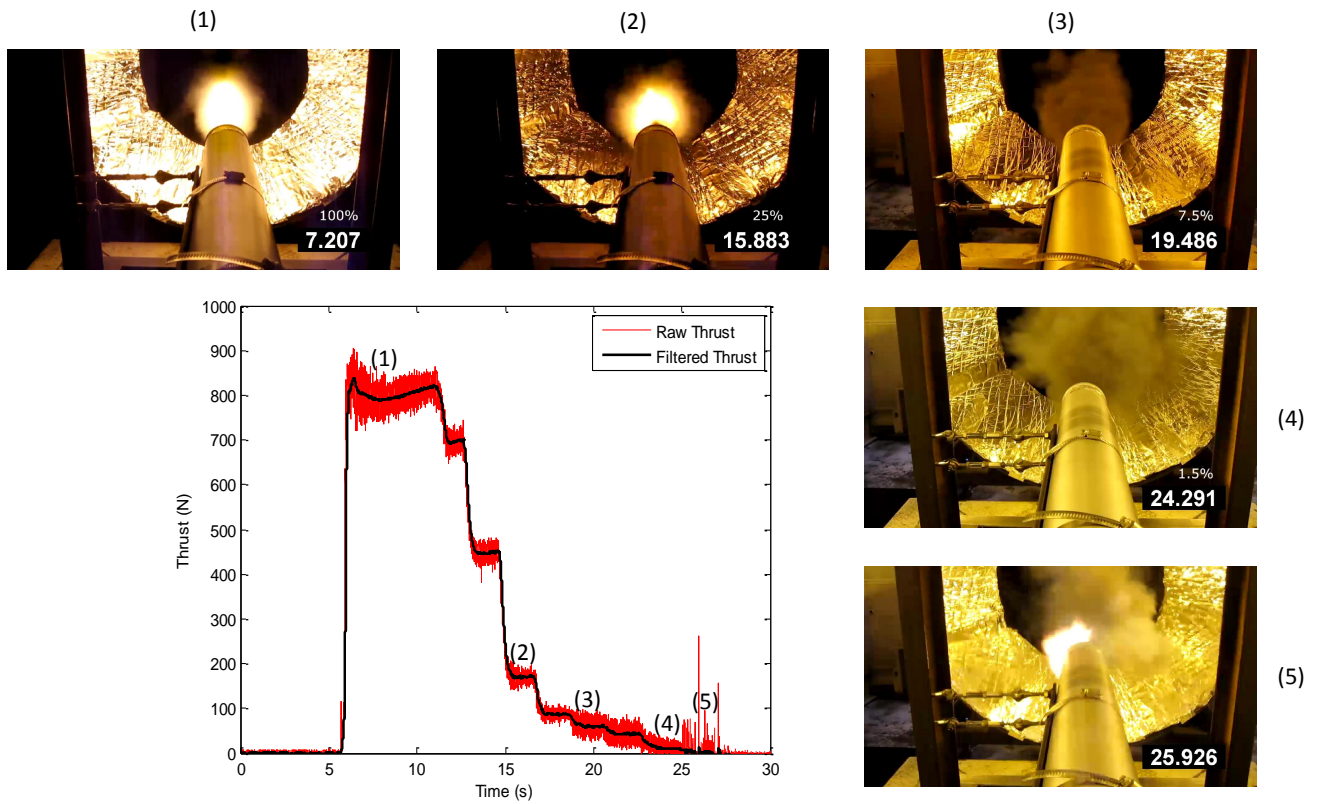


Fig. 6.7: Thrust time history with video stills from deep throttle test.

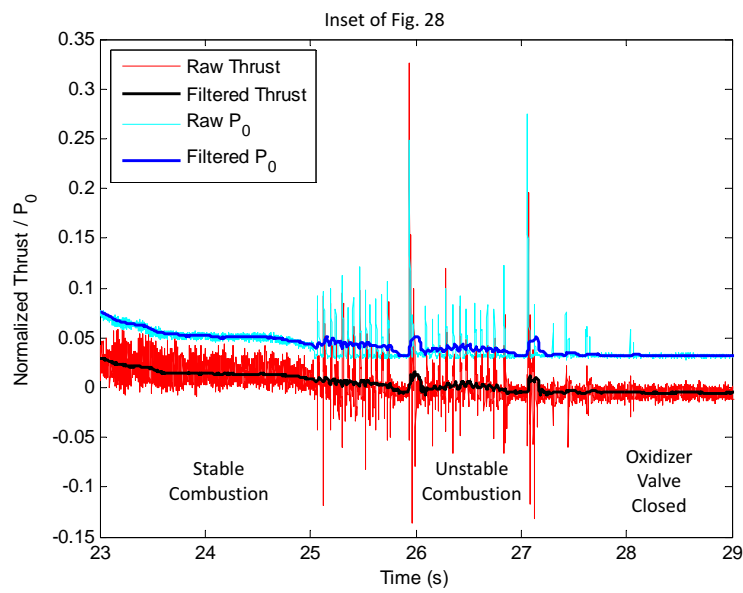


Fig. 6.8: Normalized thrust and chamber pressure during unstable combustion in deep throttle test.

tling study of the Common Extensible Cryogenic Engine (CECE) achieved a turndown ratio of 17.6:1 [60]. While liquid engines can be throttled to reasonably high turndown ratios, deep throttling of liquid systems requires a variable geometry injection system and a variable area nozzle. Proper fuel and oxidizer atomization is critical for stable combustion in liquid rockets [61]. Maintaining a sufficiently high pressure drop across the injector for satisfactory atomization sets a practical lower limit to the depth of throttling that can be achieved. Specialized injectors are required to maintain combustion stability during deep throttling. In addition to specialized injectors, specialized turbo pumps or valves are required. Turbo pumps must be designed to avoid cavitation, stalling, or surging and must have stable rotordynamics and structural dynamics for a wide flow range. Because both the fuel and oxidizer must be controlled carefully, valves are required to control flow to high degree of accuracy over a wide flow range. Regeneratively cooled liquid engines may also have insufficient heat transfer at high throttling ratios.

By contrast, the 66:1 turndown ratio demonstrated during this project was accomplished using a standard, off-the-shelf components - a ball valve to control oxidizer flow and spray nozzle for the injector. In hybrid rockets, the regression rate of the solid fuel varies nearly linearly with the oxidizer mass flow rate. The result is a self-compensating effect in the mixture of the fuel and oxidizer that greatly decreases the complexity and accuracy of the equipment required to achieve stable thrust over a wide range. Because hybrid combustion is primarily a surface phenomenon, the atomization of the oxidizer through the injector is not as critical in hybrids as it is in liquid rockets for combustion stability. The solid fuel regression rate is driven by the oxidizer mass flux in the motor, so there is a self-compensating effect in fuel mixing as the oxidizer mass flow rate drops during throttling. By contrast, if the injector pressure ratio in a liquid rocket is insufficient to fully vaporize the fuel and oxidizer they will not fully mix, leading to non-homogeneous combustion within the chamber. The conventional lower limit of injector pressure ratio in liquid engines is 1.25 to maintain stable combustion. Figure 6.9 shows that the injector pressure ratio actually increased as the hybrid motor was throttled down during the deep throttle test. The

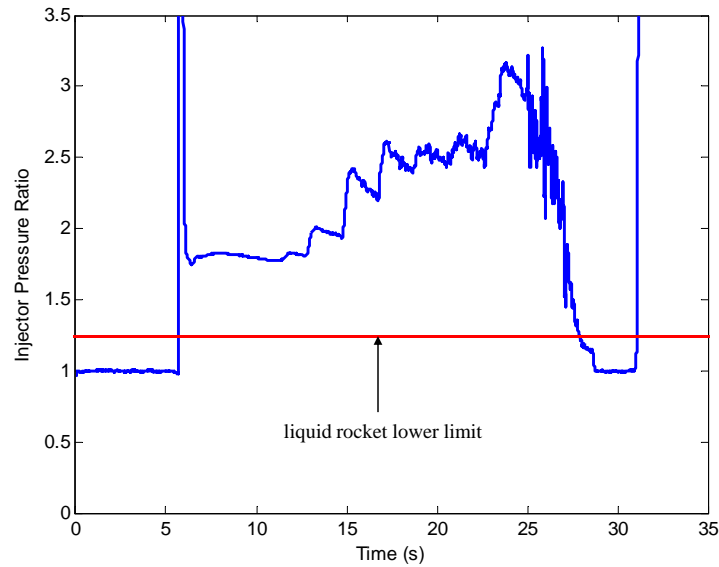


Fig. 6.9: Injector pressure ratio during deep throttle test.

only physical lower limit to hybrid rocket deep throttling is the ability to maintain positive pressure between the motor chamber and nozzle exit.

The trade-off for the ease and depth of hybrid rocket motor throttling is the loss of efficiency. Motor I_{sp} decreased significantly below 10% of peak thrust. Several techniques have been developed to counteract this drop in efficiency such as oxidizer injection near the nozzle and pressure sensitive fuels [16]. However, because this project was considered an initial evaluation and the main focus was on developing a closed-loop throttle controller, no steps were taken to improve deep throttling efficiency.

Chapter 7

Closed-Loop Throttle Testing

The final phase of throttle testing was demonstration of the closed-loop controllers. Cold-flow testing was performed first. Thrust-feedback hot-flow testing followed cold-flow testing because much of the infrastructure was the same and few changes were required to switch. Following satisfactory demonstration of thrust-feedback hot-flow testing, chamber pressure-feedback hot-flow closed-loop control was demonstrated. Table 7.1 presents a summary of successful closed-loop throttling tests.

To provide a means of comparison between tests, controller performance was rated using the integral of the absolute magnitude of the error (IAE), calculated as [55]

$$\text{IAE} = \int_0^{t_{tot}} |e(t)| dt, \quad (7.1)$$

where t_{tot} is the total run time of the controller and e is the error, defined as the difference between the sensed and command thrust signals. IAE accumulates over the duration of the test so only the first ten seconds of each test, equal to the shortest test duration, were used so that a more direct comparison could be made. The controller was run on the cFP, but data recorded on the cDAQ was used to calculate IAE to provide a semi-independent

Table 7.1: Closed-loop throttle test summary.

Test Number	Motor Name	Command Profile	Feedback	K_P	K_I	f_c	IAE (N-s)
ColdFlowCL12	n/a	step	F_t	0	1	5	70.6
ColdFlowCL13	n/a	step	F_t	0	0.75	5	93.7
ColdFlowCL14	n/a	step	F_t	0	0.85	5	96.0
HTPBCL1	A Rising Tide	step	F_t	0.4	2.0	8	355
HTPBCL2	Pink Elephant	ramp	F_t	0.4	2.0	8	422
PressHTPBCL3	Bunrake	ramp	P_0	0.4	2.5	20	305
PressHTPBCL4	The Boy	step	P_0	0.4	2.5	20	556
PressHTPBCL5	The Mistress	step	P_0	0.3	2.0	20	695

observation.

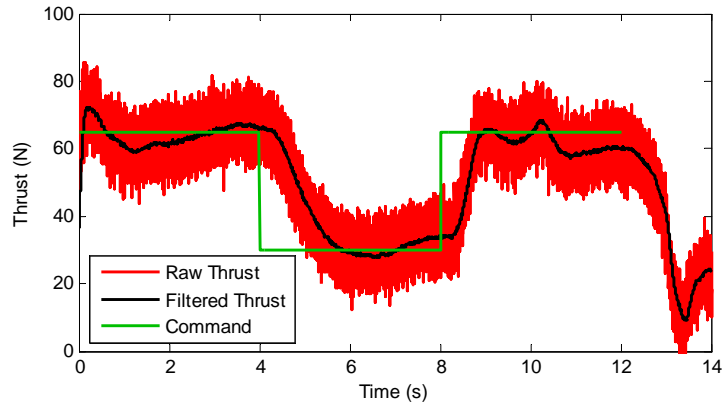
The cutoff frequency, f_c , is the value used in the lowpass filter for each controller. For thrust-feedback tests (cold-flow and hot-flow) the cutoff frequency needed to at least be below 30 Hz to avoid having the test stand structural harmonic frequency feed through the load cell into the controller. In both the cold-flow and hot-flow tests, however, the cutoff frequency was set much lower to reduce the noise amplitude. The hybrid low frequency mode was not observed in the test motor configuration, so resonance was not as much of a concern for chamber pressure-feedback tests as it was for thrust-feedback tests. As with the thrust-feedback tests, the cutoff frequency was selected mainly to reduce noise amplitude.

7.1 Cold-Flow Test Summary

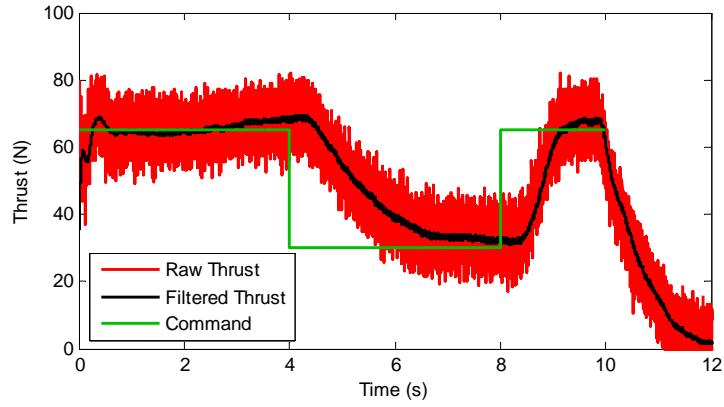
Figure 7.1 shows thrust time histories for the final three closed-loop cold-flow throttle tests. Cold-flow tests were done in series of three to four tests with minor adjustments to settings made between tests. Several tests were performed to “dial in” the cutoff frequency of the lowpass filter and gains used. Cold-flow testing showed that the gains in the controller produced a slightly less damped response than predicted by the simulator, but the cutoff frequency used in the simulator accurately reflected the cutoff frequency used in the controller. The specific reason for the difference between for the difference between damping in the simulator and in the test motor configuration is not known. Individual parameter values were tweaked in the simulator, but the damping level seen in the controller tests could not be duplicated. There is a dynamic system response that the simulator cannot duplicate, whether because it is missing entirely or because the accumulation of errors from rounding and calculation assumptions impacts the simulator’s ability to reproduce it. Integral gains were set lower than those predicted to be stable by the simulator, typically in the range of 0.75-1 instead of the 1.25-1.75 used in the simulator.

7.2 Hot-Flow Test Summary

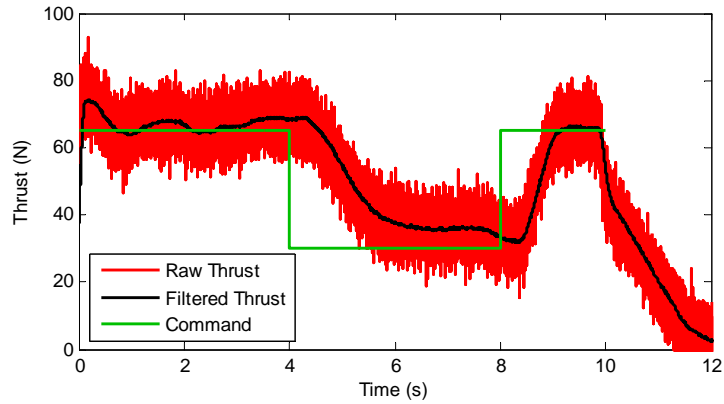
Five successful hot-flow closed-loop throttle tests were performed - two with thrust feedback and three with chamber pressure feedback. The following subsections describe



(a)



(b)



(c)

Fig. 7.1: Thrust time histories for cold-flow closed-loop tests (a) ColdFlowCL12 (b) ColdFlowCL13 and (c) ColdFlowCL14.

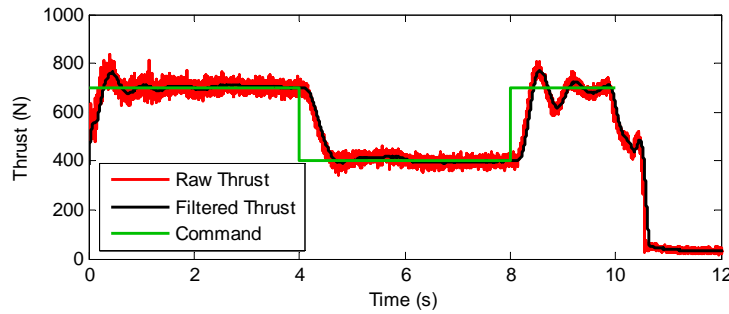


Fig. 7.2: Thrust signal compared to command for Test HTPBCL1.

the closed-loop responses of the thrust and chamber pressure feedback controllers to the prescribed step and ramp profiles.

7.2.1 Thrust-Feedback Tests

Figures 7.2 and 7.3 show the results from Tests HTPBCL1 and HTPBCL2. HTPBCL1 was a step input test with a 10 second duration. HTPBCL2 had a ramp input and a 15 second duration. Cold-flow closed-loop testing provided a reasonable analog to the hot-flow thrust-feedback tests because the same feedback mechanism was used. Both controllers performed as expected based on simulator and cold-flow test results.

The step profile tests had ringing in the controller response on the second step as Fig. 7.2 shows. On the first step the servo was initialized to a position near where it settled during the initial set point. On the second step the set point transitioned from a control region where thrust changes nearly linearly with valve position to a region where large changes in valve position produce little change in thrust. The ringing may be caused by an increasing controller signal during the transition. Changes in thrust from the nominal values due to drift over time could also have an effect. The small step at the beginning of the ramp command shown in Fig. 7.3 just before the 8 second mark is the most apparent effect of the servo deadband.

7.2.2 Chamber Pressure-Feedback Tests

Figures 7.4 through 7.6 show results from three of the chamber pressure-feedback tests.

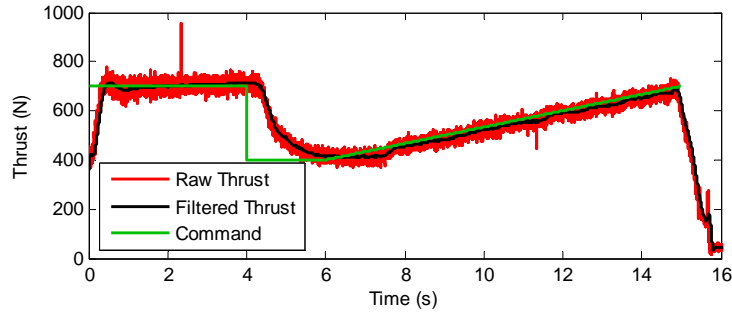


Fig. 7.3: Thrust signal compared to command for for Test HTPBCL2.

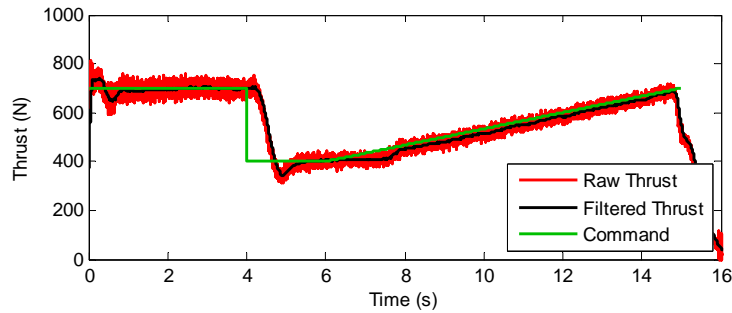


Fig. 7.4: Thrust signal compared to command for Test PressHTPBCL3.

Two additional tests were performed with more aggressive gains that proved to be unstable. PressHTPBCL3 was a ramp input test with a 15 second duration and PressHTPBCL4 and PressHTPBCL5 were both step input tests with 12 second durations. The gains used for PressHTPBCL3 were predicted by the simulator to produce approximately the same damping as those used for HTPBCL2. Comparison of Figures 7.3 and 7.4 shows that damping was higher for HTPBCL2. This was mainly due to nozzle erosion effects.

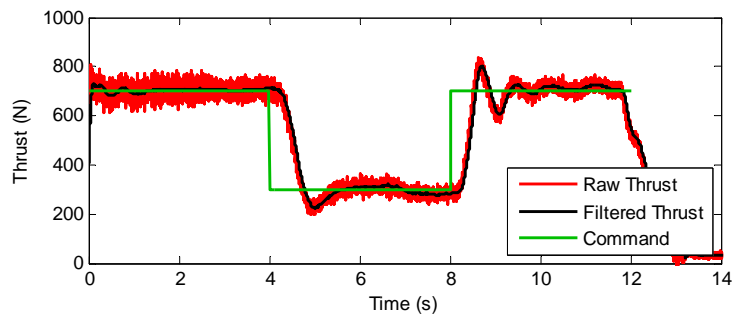


Fig. 7.5: Thrust signal compared to command for Test PressHTPBCL4.

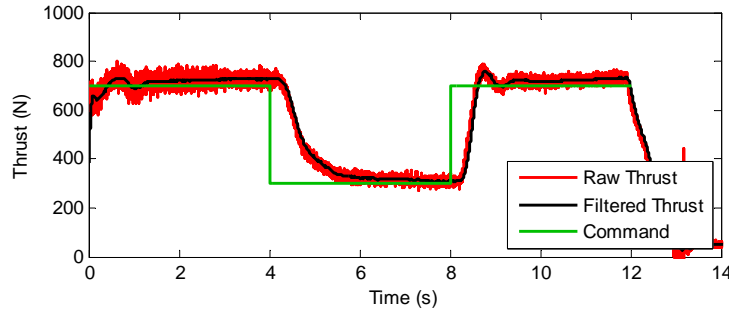


Fig. 7.6: Thrust signal compared to command for Test PressHTPBCL5.

The gains used for PressHTPBCL4 were meant to repeat the amount of damping as observed for HTPBCL1. Comparison of Figures 7.2 and 7.5 shows that this was the case. Gains were lowered for PressHTPBCL5 to reduce the amount of ringing in the controller response to the second step. Figures 7.5 and 7.6 show that the trade off for decreased ringing in the controller response is an increase in response time. The balance between oscillations and response time can be adjusted with the gains to meet mission requirements. PressHTPBCL5 exhibits an upward shift from the target thrust because of the chamber pressure-feedback controller's inability to adjust for nozzle erosion.

7.2.3 Simulator Comparison

Simulator results shown in Fig. 5.11 had the same operating conditions as PressHTPBCL4, results shown in Fig. 7.5. As with the cold-flow controller, the actual response was slightly less damped than the simulator response. This result was typical of both hot-flow controllers. Although the response was less damped, gain sets predicted to be stable by the simulator were also stable in the controllers. There was no need to reduce the gains to the extent as was necessary for the cold-flow controller, but the gains were still reduced slightly to improve controller performance.

7.2.4 Servo Deadband Effects

As discussed in Section 6.6, the servo deadband results in a small step in the servo response for ramp inputs. Figure 7.7 compares the output voltage signal from the controller

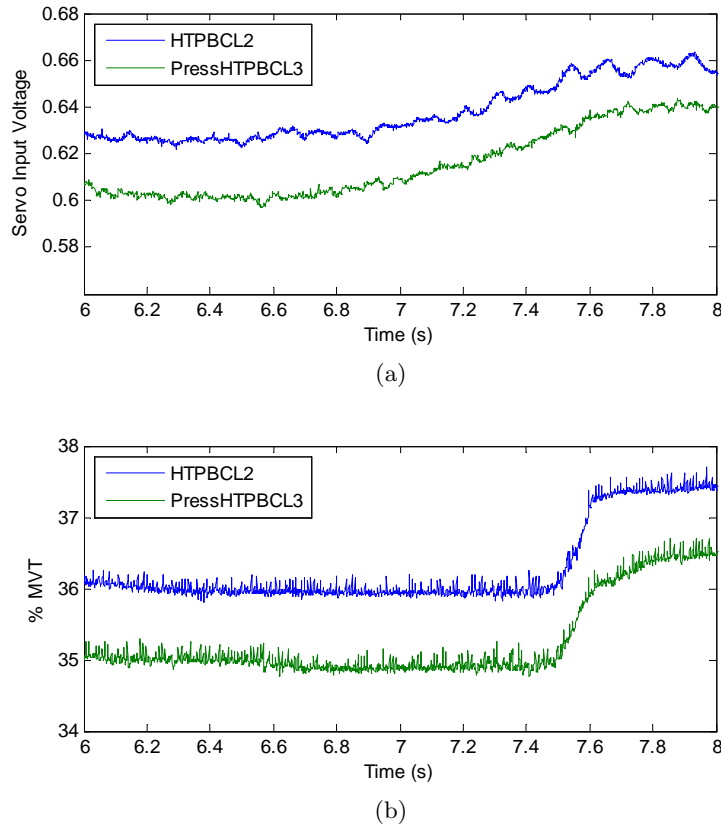


Fig. 7.7: Servo input voltage and position at beginning of ramp up command.

to the actual servo response at the beginning of the ramp input command for the two ramp-profile tests. Comparison of parts (a) and (b) of the figure shows that the ramp does not begin until the 0.02 volt deadband has been exceeded, at which point the control valve position quickly changes to match the controller output signal. The subtle dip in the servo input voltage observed in Fig. 7.7(a) is due to the controller compensating for the gradual shift in thrust over the duration of the burn. Figure 7.7(b) shows that the control valve does not respond to such subtle changes in controller output due to the deadband. The lag in the servo position response time to a ramp input voltage signal due to the servo deadband shown in Fig. 6.6 can be observed in Figures 7.3 and 7.4 as the difference in command and feedback signals during the ramp for a given time.

Table 7.2: Nozzle erosion during hot-flow throttle tests.

Test	Δd_n (mm)	ΔA_n (%)
HTPBCL1	negligible	negligible
HTPBCL2	0.10	1.2
PressHTPBCL3	negligible	negligible
PressHTPBCL4	negligible	negligible
PressHTPBCL5	0.05	0.6

7.2.5 Nozzle Erosion Effects

Following each test the nozzle was cleaned thoroughly, being careful to remove all of the soot from the motor burn while not scouring into the graphite. A bore gauge was then inserted into the nozzle at four orientations separated by approximately 45° . The bore gauge was measured at each orientation using calipers with a 0.0005 inch resolution. The average of the four measurements was assumed to be the average diameter of the nozzle throat. Two of the five tests exhibited a significant amount of nozzle erosion. Table 7.2 shows the approximate amount of nozzle erosion during each test. In the table, “negligible” means the amount of nozzle erosion was less than the resolution of the calipers used to measure the nozzle throat diameter after each test.

The thrust-feedback controller used in HTPBCL2 was able compensate for the eroded nozzle because the thrust was controlled directly. Figure 7.1 shows that the thrust from HTPBCL2 was approximately the same as the tests without nozzle erosion, while Fig. 7.8 shows that the control valve was opened substantially wider to produce the same thrust. The chamber pressure-feedback test, PressHTPBCL5, on the other hand, was unable to compensate for the change in the nominal relationship between thrust and chamber pressure using the a priori conversion discussed in Section 4.2, even though the chamber pressure remained at nominal levels. Because thrust cannot be measured directly in-flight, this problem could be encountered with any in-flight feedback mechanism. However, shifts from nominal controller operating conditions can be avoided by using an online conversion capable of compensating for changes. For example, there is a clear correlation between nozzle erosion and the valve position during the initial set point. A weighting factor could be applied to the set point based on the deviation from the nominal valve position to

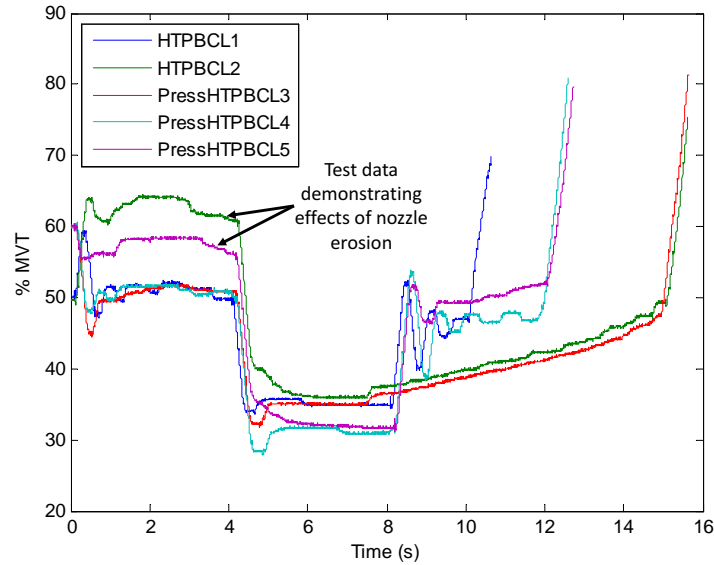


Fig. 7.8: Control valve position during hot-flow closed-loop throttling tests.

adjust for the larger nozzle diameter. These tests were performed using basic controllers and off-the-shelf equipment. A more sophisticated throttle control system should be able to easily avoid or compensate for the off-nominal operating conditions encountered during this project.

7.2.6 Steady-State Accuracy

Reducing the amount of motor-to-motor variability was the primary motivation for using closed-loop throttling instead of open-loop. The first four seconds of each of the five hot-flow throttle tests presented here had the same target thrust, 700 N. Steady-state controlled response was evaluated by calculating a mean and standard deviation of the recorded thrust for all tests in the 2-4 second time interval, avoiding the initial transients. The 95% confidence interval of the mean thrust during the initial 700 N set point was ± 27.68 N for all five controlled tests. If Test PressHTPBCL5, which used chamber-pressure feedback and had nozzle erosion, is neglected this amount reduces to ± 10.63 N, a significant reduction compared to the 95% confidence interval of ± 69.46 N for the uncontrolled motor burns shown in Fig. 4.1. The mean thrust during the initial 700 N set point for all five

tests was 1.14% higher than the set point as measured on the cDAQ, or 0.53% higher if PressHTPBCL5 is neglected.

Chapter 8

Conclusion

Hybrid rocket throttling has potential applications both in space and for use in atmospheric flight. Open-loop throttle testing established physical relationships between the control valve and motor response. Liquid rocket engines are physically limited in deep throttle by an approximate 1.25 injector pressure ratio. This limit was not observed in the hybrid rocket test motor configuration. Deep throttle testing showed that the test motor configuration could produce stable combustion in a 66:1 turndown ratio and that the injector pressure ratio increased with deeper throttling.

Closed-loop thrust-feedback throttle controllers were developed for a cold-flow nitrous oxide thruster and for a nitrous oxide/HTPB hybrid rocket motor. A closed-loop chamber pressure-feedback throttle controller was also developed for the nitrous oxide/HTPB hybrid rocket motor. Closed-loop cold-flow throttle testing was performed before hot-flow testing began to evaluate the accuracy of the simulator. Slightly smaller gains were used in the hot-flow system because damping of the simulator response was observed to be lower than in the cold-flow system controller. Reduced damping was also observed in the hot-flow controllers, but reducing gains was not necessary.

Hot-flow closed-loop controller testing showed that thrust could be controlled reasonably accurately even in the presence of nozzle erosion. The chamber pressure-feedback hot flow controller could not adjust for nozzle erosion because the conversion between thrust and chamber pressure was prescribed a priori, but still only deviated from the mean of the controlled thrust by about half of the standard deviation of uncontrolled thrust using the same motor configuration. For an in-flight system, the impact of off-nominal performance due to factors such as nozzle erosion can be limited by adding an online conversion between thrust and the feedback mechanism capable of adjusting the set point. The 95% confidence

interval for mean thrust decreased from ± 69.46 N for the uncontrolled tests to ± 27.68 N for the controlled tests. Mean thrust at a common set point for all controlled tests was within 1.14% of the target. For closed-loop throttle tests not affected by nozzle erosion, the 95% confidence interval for mean thrust was ± 10.63 N and the mean thrust was within 0.53% of the target.

All throttle controller testing was performed using basic controllers and off-the-shelf equipment. Controller performance can be improved using a more sophisticated throttle control system with features such as a control valve actuator with reduced or no deadband, a control valve with a more linear flow profile, using an automation controller capable of running higher loop frequencies, and an online, adaptable conversion between thrust and the feedback mechanism. Even with all of the hardware limitations in this experiment, the throttle control system substantially reduced the variability of the test motor configuration as compared to the uncontrolled tests.

References

- [1] Chang, I.-S., "Investigation of Space Launch Vehicle Catastrophic Failure," *AIAA Paper 95-3128*, July 1995.
- [2] Safie, F. M. and Fox, E. P., "A Probabilistic Design Analysis Approach for Launch Systems," *27th AIAA, SAE, ASME, and ASEE, Joint Propulsion Conference*, Vol. AIAA-1991-3372, 1991.
- [3] Maggie, G., "Space Shuttle Probabilistic Risk Assessment: Methodology and Application," *International Symposium on Product Quality and Integrity, Proceedings of the Reliability and Maintainability Symposium, Las Vegas NV*, 1996.
- [4] Anon., "Hazard Analysis of Commercial Space Transportation; Vol. 1: Operations, Vol. 2: Hazards, Vol. 3: Risk Analysis," *U.S. DOT, PB93-199040, Accession No. 00620693*, 1988.
- [5] Choudhary, G., Hansen, H., Donkin, S., and Kirman, C., "Toxicological Profile for Hydrazines," *US Department of Health and Human Services Public Health Service Agency for Toxic Substances and Disease Registry (ATSDR). Atlanta GA*, 1997, pp. 1–224.
- [6] DeSain, J. D., "Green Propulsion: Trends and Perspectives," *Crosslink*, <http://www.aero.org/publications/crosslink/summer2011/04.html>, [retrieved 21 March, 2012].
- [7] Anon., "Occupational Safety and Health Guideline for Nitrous Oxide," *US Department of Labor, Occupational Health and safety Administration*, <http://www.osha.gov/SLTC/healthguidelines/nitrousoxide/recognition.html>, [retrieved 28 March 2012].
- [8] Rhodes, G. W., "Investigation of Decomposition Characteristics of Gaseous and Liquid Nitrous Oxide," *Air Force Weapons Laboratory, Report AD-784 602, Kirtland AFB, New Mexico*, July 1974.
- [9] Altman, D., "Hybrid Rocket Development History," *27th AIAA, SAE, ASME, and ASEE, Joint Propulsion Conference*, 1991.
- [10] Moore, G. E. and Berman, K., "A Solid-Liquid Rocket Propellant System," *Jet Propulsion*, Vol. 26, No. 11, November 1956, pp. 965–968.
- [11] Duban, P., "The "LEX" rocket probe (LEX small rocket probe for in-flight testing of ONERA studies of hybrid propulsion, discussing design and program)," *L'Aeronautique et L'Astronautique*, 1968, pp. 47–54.
- [12] Franklin B. Mead, J. and Bornhorst, B. R., "Certification Tests of a Hybrid Propulsion System for the Sandpiper Target Missile," *AFRPL-TR- 69 -73*, 1969.

- [13] Jones, R. A., "Hybrid Propulsion System for an Advanced Rocket-Powered Target Missile," *Quarterly Technical Report, UTC 2220-QTR2*, 1967.
- [14] Penn, C. D. and Branigan, J. E., "Preliminary Flight Rating Tests of the HAST Propulsion System," *AFRPL-TR-15-5*, 1975.
- [15] "AQM-81A Firebolt," *Tactical Air Command Technical Report, Langley AFB VA*, Oct 21, 1983.
- [16] Ordahl, D., "Hybrid Propulsion," *Space Aeronautics*, Vol. 41, No. 4, April 1964, pp. 108–113.
- [17] Hamers, J., "Experimental Investigation of Prepackaged Hybrid Propellant Systems," *Final Report AFRPL-TR-67-168*, 1967.
- [18] Sutton, G. P. and Biblarz, O., *Rocket Propulsion Elements, 7th Ed.*, Wiley, New York City, NY, 2001.
- [19] French, J. R., "AMROC Industrial Launch Vehicle: A Low Cost Launch Vehicle," *SAE Technical Paper 871336*, 1987.
- [20] Kniffen, R., McKinney, B., and Estey, P., "Hybrid Rocket Development at the American Rocket Company," *AIAA-90-2762*, 1990.
- [21] Estey, P. N. and Flittie, K. J., "Aquila - The Next Generation Launch Service for Small Satellites," *14th International Communication Satellite Systems Conference and Exhibit, Washington DC*, March 22-24, 1992.
- [22] Flittie, K. J. and Estey, P., "Large-Scale Hybrid Motor Performance and Designs for use in Launch Vehicle Applications," *JANNAF Propulsion Meeting*, Vol. 2, 1993, pp. 37–50.
- [23] McFarlane, J. S., Kniffen, R. J., and Lichatowich, J., "Design and Testing of AMROC's 250,000 Pound Thrust Hybrid Motor," *AIAA/SAE/ASME/ASEE 29th Joint Propulsion Conference and Exhibit, Monterey, CA*, June 28-30, 1993.
- [24] Flittie, K. J., Estey, P. N., and Kniffen, R., "The Aquila Launch Vehicle: A Hybrid Propulsion Space Booster," *Acta Astronautica*, Vol. 28, 1992, pp. 99–110.
- [25] Schuler, A. L. and Wiley, D. R., "Hybrid Propulsion Technology Program: Phase 1, Volume 1," *NASA-CR-183972*, 1989.
- [26] Schuler, A. L. and Wiley, D. R., "Hybrid Propulsion Technology Program: Phase 1, Volume 2," *NASA-CR-183973*, 1989.
- [27] Schuler, A. L. and Wiley, D. R., "Hybrid Propulsion Technology Program: Phase 1, Volume 3," *NASA-CR-183974*, 1989.
- [28] Jensen, G. E. and Holzman, A. L., "Hybrid Propulsion Technology Program," *JANNAF Propulsion Meeting*, Vol. 2, 1990, pp. 143–157.
- [29] "Hybrid Propulsion Technology Program Final Report," *NASA-CR-183952*, 1990.

- [30] Boardman, T. A., Carpenter, R. L., Goldberg, B. E., and Shaeffer, C. W., "Development and Testing of 11- and 24-inch Hybrid Motors under the Joint Government/Industry IR&D Program," *AIAA Paper 93-2552*, 1993.
- [31] Carpenter, R. L., Boardman, T. A., Claflin, S. E., and Harwell, R. J., "Hybrid Propulsion for Launch Vehicle Boosters: A Program Status Update," *31st AIAA/ASME/SAE/ASEE Joint Propulsion Conference and Exhibit, San Diego CA*, July 10-12, 1995.
- [32] Arves, J., Gnau, M., Joiner, K., Kearney, D., McNeal, C., and Murbach, M., "Overview of the Hybrid Sounding Rocket (HYSR) Project," *AIAA 2003-5199*, 2003.
- [33] Wright, A. B., Teague, W., Wright, A. M., and Wilson, E. W., "Instrumentation of UALR Labscale Hybrid Rocket Motor," *Proc. of SPIE*, Vol. 6222, 2006.
- [34] Dyer, J., Doran, E., Dunn, Z., Lohner, K., Bayart, C., Sadhwani, A., Zilliac, G., Cantwell, P. B., and Karabeyoglu, A., "Design and Development of a 100 km Nitrous Oxide/Paraffin Hybrid Rocket Vehicle," *AIAA 2007-5362*, 2007.
- [35] Doran, E., Dyer, J., Marzona, M. T., Karabeyoglu, A., Zilliac, G., Mosher, R., and Cantwell, B., "Status Update Report for the Peregrine Sounding Rocket Project: Part III," *AIAA 2009-4840*, 2009.
- [36] Austin, B., Heister, S., Dambach, E., Wernimont, E., and Meyer, S., "Variable Thrust, Multiple Start Hybrid Motor Solutions for Missile and Space Applications," *46th AIAA/SME/SAE/ASEE Joint Propulsion Conference, Nashville TN*, July 25-28, 2010.
- [37] Eilers, S. D., Wilson, M., and Whitmore, S., "Analytical and Experimental Evaluation of Aerodynamic Thrust Vectoring on an Aerospike Nozzle," *46th AIAA/ASME/SAE/ASEE Joint Propulsion Conference and Exhibit, Nashville, TN*, 2010.
- [38] Eilers, S. D., Wilson, M. W., Whitmore, S., and Peterson, Z., "Side Force Amplification on an Aerodynamicclly Thrust Vectored Aerospike Nozzle," *47th AIAA/ASME/SAE/ASEE Joint Propulsion Conference*, 2011.
- [39] Whitmore, S. A., Peterson, Z. W., and Eilers, S. D., "Analytical and Experimental Comparisons of HTPB and ABS as Hybrid Rocket Fuels," *47th AIAA/ASME/SAE/ASEE Joint Propulsion Conference & Exhibit*, 2011.
- [40] Anon., "Liquid Rocket Valve Assemblies," *NASA-SP-8097*, 1973.
- [41] Anon., *Control Valve Handbook*, Fisher Controls International LLC, 2005.
- [42] Anon., "Flow Equations for Sizing Control Valves," *ANSI/ISA-75.01.01 (IEC 60534-2-1 Mod)-2007*, Nov. 2007.
- [43] "V-Control Ball Valve Selection Guide Technical Bulletin No. 1006," *Flow-Tek Technical Report*, Sept. 2008.

- [44] Miller, R. W., *Flow Measurement Engineering Handbook, 2nd Ed.*, McGraw-Hill Publishing Company, 1989.
- [45] Anon., “Hydroxyl Terminated Polybutadiene Resins and Derivatives,” *Sartomer Product Bulletin*, March 2006.
- [46] Anon., “PAPI 94 Product Information,” *Dow Plastics Form No. 109-00707-801XQRP*, August 2001.
- [47] Karabeyoglu, A., Stevens, J., and Cantwell, B., “Investigation of Feed System Coupled Low Frequency Combustion Instabilities in Hybrid Rockets,” *AIAA 2007-5366*, 2007.
- [48] Weast, R. C., editor, *CRC Handbook of Chemistry and Physics, 58th Ed.*, CRC Press, Inc., Cleveland, OH, 1977.
- [49] Span, R. and Wagner, W., “Equations of State for Technical Applications. I. Simultaneously Optimized Functional Forms for Nonpolar and Polar Fluids,” *International Journal of Thermophysics*, Vol. 24, No. 1, 2003, pp. 1–39.
- [50] Span, R. and Wagner, W., “Equations of State for Technical Applications. II. Results for Nonpolar Fluids,” *International Journal of Thermophysics*, Vol. 24, No. 1, 2003, pp. 41–109.
- [51] Span, R. and Wagner, W., “Equations of State for Technical Applications. III. Results for Polar Fluids,” *International Journal of Thermophysics*, Vol. 24, No. 1, 2003, pp. 111–162.
- [52] Gordon, S. and McBride, B. J., “Computer Program for Calculation of Complex Chemical Equilibrium Compositions and Applications I. Analysis,” *NASA RP-1311*, 1994.
- [53] McBride, B. J. and Gordon, S., “Computer Program for Calculation of Complex Chemical Equilibrium Compositions and Applications II. Users Manual and Program Description,” *NASA RP-1311*, 1996.
- [54] Carmicino, C., “Acoustics, Vortex Shedding, and Low-Frequency Dynamics interaction in an Unstable Hybrid Rocket,” *Journal of Propulsion and Power*, Vol. 25 No. 6, 2009, pp. 1322–1335.
- [55] Dorf, R. C. and Bishop, R. H., *Modern Control Systems, 7th Ed.*, Pearson Education, Inc., Upper Saddle River, NJ, 2008.
- [56] Anon., *LabVIEW PID Control Toolkit User Manual*, National Instruments Corporation, 2006.
- [57] Dyer, J., Doran, E., Dunn, Z., Lohner, K., Zilliac, G., and Cantwell, B., “Modeling Feed System Flow Physics for Self Pressurizing Propellants,” *AIAA 2007-5702*, 2007.
- [58] Chapra, S. C. and Canale, R. P., *Numerical Methods for Engineers, 7th Ed.*, The McGraw-Hill Companies, Inc., New York City, NY, 2006.

- [59] Bradley, M., “Space Shuttle Main Engine Off-Nominal Low Power Level Operation,” *33rd AIAA/ASME/SAE/ASEE Joint Propulsion Conference & Exhibit, Seattle WA*, July 6-9, 1997.
- [60] Giuliano, V. J., Leonard, T. G., and Lyda, R. T., “CECE: Expanding the Envelope of Deep Throttling Technology in Liquid Oxygen/Liquid Hydrogen Rocket Engines for NASA Exploration Missions,” *46th AIAA/ASME/SAE/ASEE Joint Propulsion Conference & Exhibit*, July 2010.
- [61] Betts, E. M. and Frederick, Robert A., J., “A Historical Systems Study of Liquid Rocket Engine Throttling Capabilities,” *46th AIAA/ASME/SAE/ASEE Joint Propulsion Conference & Exhibit, Nashville TN*, July 25-28, 2010.